

1 **Title page**

2 **Thermo-hydro-mechanical simulation of cooling-induced fault reactivation in Dutch geothermal**
3 **reservoirs**

4

5 Authors:

6 B. Mathur¹, H. Hofmann^{2,3}, M. Cacace², G. A. Hutka², A. Zang^{2,4}

7 ¹Friedrich-Alexander-Universität Erlangen-Nürnberg, Schloßplatz 4, 91054 Erlangen

8 ²Helmholtz Centre Potsdam GFZ - German Research Center for Geosciences, Telegrafenberg,

9 14473 Potsdam, Germany

10 ³Technische Universität Berlin, Straße des 17. Juni 135, 10623 Berlin, Germany

11 ⁴Universität Potsdam, Am Neuen Palais 10, 14469 Potsdam, Germany

12 Authors' email contact:

13 Bakul Mathur: mathurbakul@gmail.com

14 Hannes Hofmann (corresponding author): hannes.hofmann@gfz-potsdam.de

15 Mauro Cacace: mauro.cacace@gfz-potsdam.de

16 Gergő András Hutka: hutka@gfz-potsdam.de

17 Arno Zang: arno.zang@gfz-potsdam.de

18

19 **Abstract**

20 Geothermal energy is one of the most viable sources of renewable heat. However, the potential
21 risk of induced seismicity associated with geothermal operations may slow down the growth of
22 the geothermal sector. Previous research has led to significant progress in understanding fluid-
23 injection-induced seismicity in geothermal reservoirs. However, an in-depth assessment of
24 thermal effects on the seismic risk was generally considered to be of secondary importance. This
25 study aims to investigate the relative influence of temperature and key geological and
26 operational parameters on the slip tendency of pre-existing faults. This is done through coupled
27 thermo-hydro-mechanical (THM) simulations of the injection and production processes in
28 synthetic geothermal reservoir models of the most utilized and potentially exploitable Dutch
29 geothermal reservoir formations: Slochteren Sandstone, Delft Sandstone, and Dinantian
30 limestone.

31 In our study changes in the slip tendency of a fault can largely be attributed to thermo-elastic
32 effects, which confirms the findings of recent studies linking thermal stresses to induced
33 seismicity. While the direct pore pressure effect on slip tendency tends to dominate over the
34 early phase of the operations, once pore pressure equilibrium is established in a doublet system,
35 it is the additional stress change associated with the growing cold-water front around the
36 injection well that has the greatest influence. Therefore, the most significant increase in the slip
37 tendency was observed when this low temperature front reached the fault zone. The distance
38 between an injection well and a pre-existing fault thus plays a pivotal role in determining the
39 mechanical stability of a fault. A careful selection of a suitable target formation together with an
40 appropriate planning of the operational parameters is also crucial to mitigate the risk of induced

41 seismicity. Besides the well-known relevance of the in-situ stress field and local fault geometry,
42 rock-mechanical properties and operation conditions exert a major influence on induced stress
43 changes and therefore on the fault (re)activation potential during geothermal operations.

44 **1. Introduction**

45 The worldwide geothermal power capacity amounts to 15.4 gigawatts as of December 31, 2019
46 (Richter, 2019). In the Netherlands 24 geothermal doublets have been realized as of January 1,
47 2019 (Mijnlieff, 2020). The geothermal reservoirs in the Netherlands are the same as the ones
48 targeted for oil and gas. With a geothermal gradient of approximately 31°C/km and an average
49 surface temperature of 10°C (Bonte et al., 2012), the subsurface between 1.5 and 3.0 km depth is
50 considered suitable for geothermal exploitation with temperatures ranging between 60 to 100°C.

51 The majority of the installed doublets in the Netherlands target porous and permeable sandstone
52 reservoirs including the Rotliegend, the Lower Germanic Triassic and the Upper Jurassic/Lower
53 Cretaceous primarily in the West Netherlands Basin (Bekesi et al., 2020).

54 In this study, the Slochteren formation (part of the Permian deposits of the Upper Rotliegend
55 group) was selected as the primary sedimentary geothermal reservoir of interest, because it is
56 widely used for geothermal energy production and it extends throughout the Netherlands.

57 Additionally, the Delft Sandstone Member (Lower Cretaceous), as a local porous sedimentary
58 reservoir, and the Dinantian Limestone (Carboniferous) as deep fracture/karst dominated
59 geothermal reservoir were investigated in this study. The latter formation could potentially serve
60 as a target for a future Enhanced Geothermal System (EGS). Currently, no such projects are in
61 operation in the Netherlands. However, the large potential of these systems, ongoing research
62 (e.g. Moore et al., 2019; Huenges et al., 2020) and recent breakthroughs in EGS technology

63 (Norbeck et al., 2023) could lead to a future use of the Dinantian Limestone.

64 No major induced seismic events have yet been recorded in any of the Dutch geothermal sites in
65 hot sedimentary aquifers. The only reported seismicity related to geothermal operations in the
66 Netherlands are events with a maximum magnitude of 1.7 at the Californië site, which accesses a
67 deep fault zone in the Dinantian limestones (Vörös and Baisch, 2022). Nevertheless, the
68 possibility of induced seismicity inhibits an even faster development of the geothermal sector.

69 Induced seismicity refers to seismic events caused by human interventions (Foulger et al., 2018).
70 These seismic events are a direct result of changes of the stress state in the subsurface causing
71 rapid slip along a pre-existing region of weakness (faults/fractures). If the in-situ stresses are
72 close to a critical state with respect to the orientation of major faults, even a relatively small
73 change in stresses may lead to seismic (or aseismic) failure of a fault.

74 In this study, coupled thermo-hydro-mechanical (THM) simulations were carried out to analyse
75 the impact of various geological and operational parameters on the failure potential of a pre-
76 existing fault in typical Dutch geothermal reservoirs. The THM computations were performed
77 with the multi-physics, multi-component open source simulator GOLEM (Jacquey et al., 2017 and
78 Cacace and Jacquey, 2017). The relative influence of key geological and operational parameters
79 on the slip tendency of preexisting faults was investigated with a sensitivity analysis in a synthetic
80 geothermal reservoir model of the Slochteren Sandstone formation, the Delft Sandstone
81 formation and the Dinantian Limestone formation in the Netherlands. Among those parameters,
82 a focus of our study is on the effect of re-injection temperature and related stress changes on
83 fault stability, which likely plays a major, yet often ignored, role in injection-induced seismicity
84 (Ghassemi et al., 2007; De Simone et al., 2013; Wassing et al., 2021; Kivi et al., 2022).

85 **2. Numerical Approach**

86 The simulation code GOLEM uses a Galerkin Finite Element technique to solve for the parallel
87 implicit non-linear coupled initial-boundary value problem. Balance equations of fluid and solid
88 mass, heat and momentum serve as the base for the numerical formulations of the governing
89 equations for fluid-flow, heat transport and elastic deformation (Cacace and Jacquey, 2017).

90 **Darcy's law** correlates the Darcy's flow rate per unit of surface area or Darcy velocity (\mathbf{q}_D) with
91 porosity (n), fluid velocity (\mathbf{v}_f) and solid velocity (\mathbf{v}_s) and by expansion with the reservoir
92 permeability (\mathbf{k}), fluid viscosity (μ_f), pore-fluid pressure (p_f), fluid density (ρ_f) and acceleration
93 due to gravity (\mathbf{g}).

$$(1) \quad \mathbf{q}_D = n(\mathbf{v}_f - \mathbf{v}_s) = -\frac{\mathbf{k}}{\mu_f} \cdot (\nabla p_f - \rho_f \mathbf{g})$$

94 **The mechanical governing equation** is given by

$$(2) \quad \nabla \cdot (\boldsymbol{\sigma}' - \alpha p_f \mathbf{I}) + \rho_b \mathbf{g} = 0$$

95 where $\boldsymbol{\sigma}'$ denotes the effective stress, α denotes the Biot's coefficient of the reservoir rock,
96 ρ_b denotes the bulk density of the rock-fluid system and \mathbf{I} is an identity matrix. The effective
97 stress is given by Equation (3).

$$(3) \quad \boldsymbol{\sigma}' = \boldsymbol{\sigma} + \alpha p_f \mathbf{I}$$

98 The change in the effective thermal stress for non-isothermal deformation is proportional to the
99 drained thermal expansion coefficient (β_d), the material stiffness matrix (\mathbf{C}) and the change in
100 temperature (ΔT).

$$(4) \quad \Delta \boldsymbol{\sigma}'_T = \frac{1}{3} \mathbf{C} \beta_d \Delta T \mathbf{I}$$

101 **The equation of internal energy conservation** consists of the temporal, convective and
102 conductive parts.

$$(5) \quad (\rho c)_b \frac{\partial T}{\partial t} + (\rho c)_f q_D \nabla T - \nabla \cdot (\lambda_b \nabla T) = 0$$

103 where $(\rho c)_b$ denotes the bulk specific heat, $(\rho c)_f$ is the fluid specific heat, and λ_b denotes
 104 bulk thermal conductivity.

105 The problem variables are pore fluid pressure, temperature and solid displacement, which results
 106 in a system of non-linear coupled equations. A detailed derivation of the formulations is
 107 described in Cacace & Jacquey (2017). A weighted residual method is then applied to the system
 108 of equations to obtain the weak forms of these governing equations. The weak forms of the
 109 governing equations are solved either by Newton-Raphson or Free Jacobian Inexact Newton
 110 Krylow schemes (Cacace & Jacquey, 2017).

111 **The fault failure potential** is estimated in terms of a parameter referred to as ‘slip tendency’ (ST)
 112 which is defined as the ratio of the resolved shear stress (τ) and the effective normal stress ($\sigma'_n =$
 113 $\sigma_n - p_f$) on the fault plane (Morris et al., 1996 and Ramsay et al., 2000).

$$(6) \quad ST = \frac{\tau}{\sigma'_n}$$

114 The Mohr-Coulomb criterion is used to determine the failure of a fault plane. It states that slip
 115 occurs when the shear stress along the fault plane exceeds the static shear strength of the fault,
 116 which is given in terms of the fault friction coefficient (μ_s) and cohesion (S_o) as follows

$$(7) \quad \tau \geq S_o + \mu_s \cdot \sigma'_n$$

117 For a cohesionless fault ($S_o = 0$) slip occurs when

$$(8) \quad ST \geq \mu_s$$

118 In this study, the static friction coefficient of the fault was taken as 0.6. A slip tendency value higher
 119 than 0.6 was therefore considered as an indication of fault failure.

120 We note that the slip tendency only gives a probability of (re)activation of the fault without
 121 providing information on whether the resulting fault is seismic or aseismic. Therefore, we
 122 performed an additional study, considering a rate and state formalism to describe the frictional

123 behaviour of the fault, which we discuss in the supplementary text (Figures S1-S4). In addition, we
124 refer to a companion study by Hutka et al. (2023) that uses the same model geometry and a
125 different method introduced by Cacace et al. (2021) to quantify the seismic response of the
126 reservoir in the same scenarios presented in this study.

127 **3. Model setups and scenarios**

128 The THM simulation including slip tendency analysis with GOLEM has been validated at the Groß
129 Schönebeck (GrSk) Enhanced Geothermal System (EGS) site (Blöcher et al., 2018). This site
130 accesses the Rotliegend formation below ~3900 m.

131 The validated model was adapted to the condition in the different formations of interest in the
132 Netherlands. All reservoir models were setup in a similar fashion. The coordinates of the model
133 were aligned with the maximum (S_{HMax}) and minimum horizontal stress directions (S_{Hmin}). This
134 was done to avoid any shear stress accumulation along the edges of the model and the resulting
135 distortion of the original model geometry. The Finite Element mesh was generated with the open
136 source software MeshIt (Cacace et al., 2015). Mesh refinement was applied around the
137 wellbores, along the fault and inside the reservoir unit. We used an adaptive time stepping,
138 where the time step size increases with the number of nonlinear iterations at each time step with
139 an upper bound of 1 year. A steady state simulation run first to initialize the model in terms of
140 pore pressure, temperature and relative displacements, consistent with the in-situ reservoir
141 conditions. This steady state model was then used as starting model (initial conditions) for the
142 subsequent transient runs covering a 30-year simulation period with cold water injection and
143 production with the same flow rate.

144 **3.1. Slochteren sandstone reservoir**

145 The Slochteren sandstone model was simplified to three horizontal geological units: Zechstein
146 (top seal unit), Slochteren (reservoir unit) and Limburg (bottom seal unit). All three units are
147 intersected by a two-dimensional fault. The two wells are represented by one-dimensional line
148 elements representing the open hole sections of the injection and production well, which
149 intersect the entire reservoir unit. Figure 1 illustrates the top and side views of the Slochteren
150 base case model. Figure 2 is a snapshot of the base case model mesh. Mechanical, hydraulic and
151 thermal properties of the rock matrix of reservoir, top and bottom unit as well as fault properties
152 can be found in Table 1. Fluid properties are summarized in Table 2. A summary of the model
153 geometry and wellbore information is provided in Table 3. Detailed information on the adopted
154 boundary conditions are presented in Table 4.

155 **3.1.1. Model geometry and boundary conditions**

156 The top of the Slochteren reservoir varies between 1500 m and 3000 m and its thickness varies
157 between 100 m and 250 m (Mijnlieff, 2020). We chose the Middenmeer site with a top
158 Slochteren depth of 2200 m and a thickness of 200 m as representative for the base case model
159 (DESTRESS, 2021). The thickness of the overlying Zechstein group varies between <100 m (in
160 marginal settings) and >1200 m (in the salt basin; TNO-GSN, 2021a; Duin et al., 2006). The
161 underlying Limburg group has typically a thickness of ~600 m which can reach up to 1300 m
162 (Dinoloket, 2021). To avoid any boundary effects, we used a 1000 m thickness for both top and
163 bottom layer.

164 Fault patterns are relatively homogeneous across the whole onshore part of the Netherlands
165 with a main fault trend varying between NW-SE and NNW-SSE and faults dipping in different
166 directions (Duin et al., 2006; de Jager, 2007). We do not consider secondary fault systems, that

167 strike in different directions and we consider only a dip towards NE. Cross-sections in de Jager
168 (2007) show that most faults are sub-vertical. Thus, we assume a typical fault dip of 80° and
169 tested variations in the dip angle between 60 and 85° .

170 The average temperature gradient in the Netherlands can be considered as $31^\circ\text{C}/\text{km}$ with a
171 surface temperature of 10°C and an uncertainty of $\pm 10^\circ\text{C}/\text{km}$ (Bonté et al., 2014). We therefore
172 use $31^\circ\text{C}/\text{km}+10^\circ\text{C}$ for the base case, $20^\circ\text{C}/\text{km}+10^\circ\text{C}$ as minimum and $40^\circ\text{C}/\text{km}+10^\circ\text{C}$ as maximum
173 temperature gradient. Despite the possibility of local fluid overpressures (Verweij et al., 2012),
174 we assume an initial hydrostatic pore pressure gradient in our simulations. For this, we assume a
175 minimum density of $1020\text{ kg}/\text{m}^3$, representative for seawater, and a maximum density of 1220
176 kg/m^3 , representative for a brine with salinity of $\sim 400\text{ g}/\text{l}$, which is rarely exceeded in the Dutch
177 Rotliegend (Veldkamp et al., 2016). This corresponds to minimum and maximum pore pressure
178 gradients of 10 and $12\text{ MPa}/\text{km}$. For the base case scenario, we chose $11\text{ MPa}/\text{km}$, representative
179 for the GrSk geothermal site with $265\text{ g}/\text{l}$ salinity (Blöcher et al., 2010).

180 We assume a normal faulting regime ($S_V > S_{H_{\text{max}}} > S_{H_{\text{min}}}$) according to Guises et al. (2015).
181 According to Verweij et al. (2016) the vertical stress gradient in the Netherlands is frequently
182 below the standard gradient of $\sim 23\text{ MPa}/\text{km}$ (corresponding to $\sim 2300\text{ kg}/\text{m}^3$ bulk density). Van
183 Eijs (2015) shows vertical stress gradients increase with depth from $\sim 19\text{--}21\text{ MPa}/\text{km}$ at 1 km
184 depth to $22\text{--}24\text{ MPa}/\text{km}$ (at 3 km depth). We therefore assume an average vertical stress gradient
185 of $22\text{ MPa}/\text{km}$ for the base case scenario with a possible variation between $21\text{ MPa}/\text{km}$ and 23
186 MPa/km . Note that these are average gradients over the entire depth range and only the
187 corresponding effective horizontal stress values at a point located at the center of the Slochteren
188 formation are used for model calibration. The actual stress gradients in the individual layers

189 depend on the elastic rock properties.

190 According to TNO (2015), the standard minimum horizontal stress gradient can be considered as

191 0.6 times the standard vertical gradient of 23 MPa/km ($\Delta S_{hmin}=13.8$ MPa/km). They find that the

192 leak-off pressure, which is representative for the minimum horizontal stress, is rarely below this

193 standard gradient and is also bound by the lithostatic stress gradient. Osinga and Buik (2019)

194 propose a S_{hmin} gradient of 18 MPa/km for the deeper Dinantian formation. Guises et al. (2015)

195 determined minimum horizontal stress gradients of 15.4-16.7 MPa/km for the Groningen gas

196 field. We assume a minimum horizontal stress gradient of 14 MPa/km for the base case scenario

197 with 13 MPa/km and 20 MPa/km as lower and upper bound, respectively.

198 Van Eijs (2015) found relatively low differences between the minimum and maximum horizontal

199 stress gradients in the Groningen gas field. Different methods yield a variation of the ratio

200 S_{Hmax}/S_{hmin} between 1.02 and 1.42. Osinga and Buik (2019) suggested S_{Hmax} as ~5-20%

201 higher than S_{hmin} as a reference. Guises et al. (2015) determined maximum horizontal stress

202 gradients of 17.3-18.2 MPa/km for the Groningen gas field. We assume a typical S_{Hmax}/S_{hmin}

203 ratio of 1.07 for the base case scenario ($\Delta S_{Hmax}=1.07*14$ MPa/km=15 MPa/km), a lower bound

204 for the S_{Hmax} gradient equal to the minimum horizontal stress gradient (14 MPa/km) and an

205 upper bound of the S_{Hmax} gradient equal to 20 MPa ($\Delta S_{Hmax}=1.42*14$ MPa/km=20 MPa/km).

206 Note that S_{Hmax} has the largest uncertainty among all stress magnitudes.

207 According to Mechelse (2017), the pre- and post-salt stress directions are similar. The maximum

208 horizontal stress direction in the Netherlands is typically NW-SE with values ranging between

209 N130°E and N5°E (Heidbach et al., 2016). Guises et al. (2015) determined the maximum

210 horizontal stress direction to be N160°E in the Groningen gas field. We assume N160°E for the

211 base case scenario and a typical range between N150°E and N170°E for the sensitivity analysis.

212 Note that stress directions may strongly vary locally since stress rotations can be expected near

213 salt domes and fault zones, which we do not consider in our sensitivity analysis.

214 According to Mijnlief (2020) the flow rate of geothermal wells accessing the Slochteren reservoir

215 ranges from ~40 to ~100 l/s. We chose these values as lower and upper limits, respectively, and

216 their median value of 70 l/s as representative for the base case scenario.

217 The well spacing (distance between production and injection well) is typically calculated as to

218 avoid thermal breakthrough during the projected lifetime of the doublet. The well spacing of

219 Dutch geothermal doublets is up to 1.5 km (Mijnlief, 2020). We therefore use 1.5 km as

220 maximum well spacing. For the base case, we use a typical well spacing of 1 km and 0.5 km

221 represents our lower bound for the sensitivity analysis.

222 Typically, a re-injection temperature of 25-35°C can be assumed for Dutch geothermal wells

223 (Hurter and Schellschmidt, 2003; Wang et al., 2019; Willems et al., 2017). We use a re-injection

224 temperature of 30°C for the base case scenario. To evaluate the effect of the re-injection

225 temperature we use 20°C and 70°C as lower and upper bound.

226 We do not model the entire geothermal wellbores explicitly but approximate them as open 1D

227 elements going through the entire reservoir layer. Therefore, we do not consider the wellbore

228 diameter in our sensitivity analysis. However, we use a typical geothermal wellbore diameter of 8

229 ½" for the open hole section in all models.

230 We use a relatively short distance between wells and fault of 250 m for the base case scenario in

231 order to easily see effects of different parameters on the temperature, pressure and stress

232 distribution on the fault. For the sensitivity analysis we vary this distance between 0 m (well

233 intersects the fault) and 1000 m.

234 **3.1.2. Rock matrix, fault and fluid properties**

235 **Geomechanical rock properties**

236 *Solid bulk modulus*

237 The Slochteren reservoir sandstone primarily consists of quartz. According to Schmitt (2015) the
238 solid bulk modulus of Quartz is 37.8 GPa (α -Quartz) and 42.97 GPa (β -Quartz). We assume a solid
239 bulk modulus of 40 GPa for the Rotliegend sandstone in the base case model. The Zechstein
240 group may consist of Calcite, Dolomite, Anhydrite and Halite with a solid bulk modulus of 73.3
241 GPa, 94.9 GPa, 54.9 GPa and 24.9 GPa, respectively (Schmitt, 2015). We assume a solid bulk
242 modulus of 30 GPa for the Zechstein formation in the base case model. Claystones, which we
243 assume representative for the Carboniferous in our model, primarily consist of Illite, Smectite
244 (Montmorillonite) and Kaolinite. The solid bulk modulus of Muscovite, dry Na Montmorillonite,
245 wet Montmorillonite and Kaolinite is 58.2 GPa, 82 GPa, 36 GPa, and 71.1 GPa, respectively
246 (Schmitt, 2015). We assumed a solid bulk modulus of 50 GPa, representative for clay according to
247 Delage (2013) for the Carboniferous Limburg claystone formation.

248 *Young's modulus and Poisson's ratio*

249 Lele et al. (2015) performed a geomechanical modeling study of the Groningen gas field.
250 For the Rotliegend reservoir Lele et al. (2015) use a porosity dependent Young's modulus and
251 Poisson's ratio with values of 10 GPa and 0.18, respectively, at 20% porosity and a variation
252 between 1 GPa and 35 GPa and between 0.05 and 0.25, respectively. Zang et al. (1996)
253 determined the Young's modulus of several Flechtingen Sandstone samples and found values
254 between 14 GPa and 29 GPa for dry samples and between 12 GPa and 24 GPa for wet samples.

255 Pijnenburg et al. (2019) determined Young's moduli between 3 and 22 GPa for Slochteren
256 Sandstone depending on the porosity and the effective confining pressure. They also find typical
257 values for Poisson's ratio close to 0.2. We therefore assume base case values for the Slochteren
258 sandstone unit of $E=10$ GPa and $\nu=0.2$ with upper and lower bounds between 3 and 30 GPa for
259 Young's modulus and 0.1 and 0.25 for Poisson's ratio.

260 For the Zechstein Halite Lele et al. (2015) use a Young's modulus of 30 GPa and a Poisson's ratio
261 of 0.35 while they use a Young's modulus of 40 GPa and a Poisson's ratio of 0.2 for the
262 Carboniferous. We use the same parameters for the base case model in our study except for the
263 Poisson's ratio of the Zechstein, where we used 0.3 for consistency with the Biot coefficient α .

264 *Biot coefficient*

265 Biot's coefficient α is not a direct parameter assigned to the model, but it is computed internally
266 as a function of the drained bulk modulus $K=E/(3(1-2\nu))$ (with Young's modulus E and Poisson's
267 ratio ν) and solid bulk modulus K_s (measured), as: $\alpha=1-K/K_s$. Using these formulas, we determined
268 the drained bulk modulus and the Biot coefficient in Table 1 and checked all values for internal
269 consistency and consistency with literature values.

270 For the Slochteren Sandstone model this yields a Biot coefficient of 0.86 for the base case model
271 and a range between 0.5 and 0.97. This is consistent with the values used by Lele et al. (2015).

272 Based on laboratory experiments, Zhang et al. (2018) found that rock salt may actually show a
273 weak poromechanical behaviour corresponding with relatively low values of the Biot coefficient
274 in the order of 0.2-0.3. Missal (2019) reported a Biot coefficient of intact rock salt of ~ 0.4 and
275 that of damaged rock salt as ~ 1 . However, Biot's coefficient of rock salt may be as low as 0.12
276 according to Kansy (2007). Using a solid bulk modulus of 30 GPa, a Young's modulus of 30 GPa,

277 and a Poisson's ratio of 0.3 yields a Biot coefficient of 0.17 for the Zechstein, consistent with a
278 low-porosity rock salt formation.

279 The Biot coefficient of the Limburg group is difficult to assess. However, the Young's modulus of
280 40 GPa, Poisson's ratio of 0.2 and solid bulk modulus of 50 GPa yield a Biot coefficient of 0.56 for
281 the Limbourg group (claystone). Both elastic properties of the Zechstein and Limburg groups may
282 vary significantly depending on the local mineralogical composition.

283 **Hydraulic rock properties**

284 *Porosity and permeability*

285 The (horizontal) permeability of the exploited Rotliegend reservoirs is between 50 and 350 mD
286 according to Mijnlief (2020). Given that a minimum transmissivity (permeability*thickness) of 10-
287 15 Dm is required for a successful project (Mijnlief, 2020) and considering a typical thickness of
288 200 m, we assume 100 mD as a representative base case scenario, corresponding to 20 Dm
289 transmissivity. However, the vertical permeability is typically 2 to 10 times lower compared to the
290 horizontal permeability (e.g., Doddema, 2012; Mohammed, 2020). We use a ratio between
291 horizontal and vertical permeability of 2 for the base case scenario and a range between 1 and 10
292 in the sensitivity analysis. According to Lele et al. (2015) and Pijnenburg et al. (2019) Rotliegend
293 sandstone porosity may range approximately between 10 and 30 %. We use 20% for the base
294 case scenario. Both Zechstein rock salt and Limburg claystone can be considered as nearly
295 impermeable formations. Therefore, we assume a horizontal and vertical permeability of 0.001
296 mD and a porosity of 1% for both formations.

297 **Thermophysical rock properties**

298 *Thermal conductivity*

299 For the Rotliegend reservoir Dianiliidis et al. (2016) use a wet thermal conductivity of 2.9 W/m/K.
300 Doddema (2012) found values for sandstone mostly between ~2.5 W/m/K and ~3.5 W/m/K and
301 used 3.0 W/m/K as wet heat conductivity of the Rotliegend reservoir layer. Considering a porosity
302 of 20% and a thermal conductivity of 0.63 W/m/K (water at 20°C) one arrives at solid heat
303 conductivities between ~3 W/m/K and 4.2 W/m/K. Blackwell and Steele (1989) provide thermal
304 conductivity values of sandstones between 2.5 and 4.2 W/m/K. Fuchs et al. (2015) report thermal
305 conductivity values of 7.7 W/m/K for quartz, 2-2.33 W/m/K for micas, and 1.9-2.25 W/m/K for
306 feldspars. We assume a solid heat conductivity of the Slochteren sandstone reservoir of 3.5
307 W/m/K with a possible range between 3.0 W/m/K and 7.7 W/m/K.

308 The thermal conductivity of halite crystals is ~5.5 W/m/K at 50°C. It varies between ~4.5 W/m/K
309 at 100°C and ~6 W/m/K at 25°C (Urquhart and Bauer, 2015). Fuchs et al. (2015) even report 6.5
310 W/m/K for Halite. Dianiliidis et al. (2016) use a wet heat conductivity of 3.5 W/m/K for the
311 Zechstein salt in their model while Doddema (2012) use a value of 5.5 W/m/K. We assume a solid
312 thermal conductivity of 4.5 W/m/K for the Zechstein salt layer.

313 The Limburg layer is assumed to consist preferentially of claystone in our model. Clays have
314 thermal conductivities between 1.8-1.85 W/m/K (Montmorillonite and Illite) and 2.7 W/m/K
315 (Kaolinite) according to Fuchs et al. (2015). Dianiliidis et al. (2016) use a wet heat conductivity of
316 2.65 W/m/K and Doddema (2012) uses 2.0 W/m/K for the Limburg group. While claystone
317 thermal conductivities are ~2 W/m/K in the literature study of Doddema (2012), they also find
318 higher values of 2.5 – 4 W/m/K for the Carboniferous. We assume a thermal conductivity of 2.0
319 W/m/K for the Limburg group.

320 *Solid heat capacity*

321 The heat capacity of quartz generally increases with temperature. Waples and Waples (2004)
322 report a solid heat capacity of quartz of 740 J/kg/K at 20°C. Feldspars have heat capacities of 630-
323 800 J/kg/K at 20°C (Waples and Waples, 2004) and plagioclase has a heat capacity between 711
324 and 837 J/kg/K at 20°C (Waples and Waples, 2004). For Quartzite and Microquartzite Waples and
325 Waples (2004) report values of 1013 J/kg/K and 950 J/kg/K at 20°C. Daniilidis et al. (2016) use a
326 heat capacity of 827 J/kg/K for their Rotliegend reservoir model and Doddema (2012) use 870
327 J/kg/K with a range of values determined from literature sources mainly between ~700 J/kg/K
328 and ~1050 J/kg/K for sandstones. Given that our reservoir has an elevated temperature, we
329 assume a base case solid heat capacity of the Slochteren sandstone reservoir of 830 J/kg/°C with
330 possible values between 650 and 1050 J/kg/°C.

331 The solid heat capacity of halite crystals lies between 1920 J/m³/K (885 J/kg/K) and 2050 J/m³/K
332 (945 J/kg/K) with no temperature dependence (Urquhart and Bauer, 2015). Waples and Waples
333 (2004) report a solid heat capacity of 926 J/kg/K at 25°C. Daniilidis et al. (2016) and Doddema
334 (2012) adopt a heat capacity of 1050 J/kg/K in their model of the Zechstein salt layer (combined
335 heat capacity of solid and fluid). We use a solid heat capacity of 925 J/kg/K for the Zechstein
336 layer.

337 The heat capacity of clay is 860 J/kg/K at 20°C according to Waples and Waples (2004). Daniilidis
338 et al. (2016) use a heat capacity of 840 J/kg/K for the Limburg formation and Doddema (2012)
339 used a value of 870 J/kg/K for the Carboniferous. We therefore assume a solid heat capacity of
340 860 J/kg/K for the Limburg formation.

341 *Thermal expansion coefficient*

342 The volumetric solid thermal expansion coefficient is approximately three times the linear solid

343 thermal expansion coefficient for isotropic rocks and minerals. The undrained bulk thermal
344 expansion coefficient can be expressed as $\alpha_{bu} = \alpha_s + \Phi B(\alpha_f - \alpha_s)$, with porosity Φ , Skempton
345 coefficient B , solid (mineral) volumetric thermal expansion coefficient α_s and the volumetric
346 thermal expansion coefficient of the fluid α_f (McTigue, 1986). This would be representative of
347 heating or cooling of rock with isolated (non-connected) pore space. In our model this is
348 representative for the top seal (Zechstein) and the basement (Limburg). Since the porosity of
349 these formations is negligible (1%) the effective bulk thermal expansion coefficient of the rock
350 can be considered approximately equal to the solid volumetric thermal expansion coefficient.
351 The drained bulk thermal expansion coefficient of a fluid-saturated rock is equal to the bulk
352 thermal expansion coefficient of dry rock (Jaeger et al., 2007). . The drained bulk thermal
353 expansion coefficient is representative for a porous and permeable geothermal sandstone
354 reservoir, in our case the Slochteren sandstone reservoir. The drained volumetric bulk thermal
355 expansion coefficient can be determined in the laboratory. The solid grain volumetric thermal
356 expansion coefficients are also known.

357 The effect of the thermal expansion on the pore pressure is governed by the difference between
358 the thermal expansion coefficients of pore fluid α_f and pore volume α_p (Zimmerman, 2010). This
359 coupling is neglected in our simulations.

360 The volumetric thermal expansion coefficient of quartz is equal to $33.4e-6$ $1/^\circ\text{C}$ (Palciauskas and
361 Domenico, 1982). At higher temperatures this value slightly increases ($37.2e-6$ $1/^\circ\text{C}$ at 80°C based
362 on Falzone and Stacey, 1982). The average thermal expansion coefficient of feldspars is $11.1e-6$
363 $1/^\circ\text{C}$ (Fei, 1995), the solid thermal expansion coefficient of clay is $34e-6$ $1/^\circ\text{C}$ (McTigue, 1986) and
364 the solid thermal expansion coefficient of salt is between $120e-6$ $1/^\circ\text{C}$ (McTigue, 1986) and $140e-$

365 6 1/°C (Skinner, 1966). For calcite, similar values are reported as for quartz (Srinivasan, 1955).
366 Somerton (1992) report a linear thermal expansion coefficient of Quartz of 16 e-6 1/°C and linear
367 thermal expansion coefficients of Berea, Bandera and Boise sandstone of 15e-6 to 16e-6 1/°C
368 under dry conditions and 13e-6 to 20e-6 1/°C under saturated conditions. The drained bulk
369 volumetric thermal expansion coefficient of Rothbach sandstone was measured as 28e-6 1/°C
370 and calculated as 29.7e-6 1/°C by Ghabezloo and Sulem (2009). Hassanzadegan et al. (2012)
371 determined a solid volumetric thermal expansion coefficient of a 10% porosity Flechtinger
372 Sandstone to be 27.2e-6 1/°C. Plevová et al. (2011) determined thermal expansion coefficients of
373 different Czech sandstones to be ~20e-6 1/°C. Zoback (2007) reports linear thermal expansion
374 data from Griffith (1936). These values include ~10e-6 1/°C ($\alpha_v \sim 30e-6$ 1/°C) for Sandstones, ~11e-
375 6 1/°C ($\alpha_v \sim 33e-6$ 1/°C) for Quartzites and Cherts, ~6.5e-6 1/°C ($\alpha_v \sim 19.5e-6$ 1/°C) for Andesites
376 and ~8e-6 1/°C ($\alpha_v \sim 24e-6$ 1/°C) for Slates. Zoback (2007) states that the linear thermal expansion
377 coefficient of silica is ~10e-6 1/°C ($\alpha_v \sim 30e-6$ 1/°C) while it is ~1e-6 1/°C ($\alpha_v \sim 3e-6$ 1/°C) for most
378 other rock forming minerals. Slizowski et al. (2015) determined volumetric thermal expansion
379 coefficients of 43e-6 to 54e-6 1/°C for polish Zechstein salt aggregates in laboratory experiments
380 for the temperature range 20-100°C. The volumetric thermal expansion coefficient of anhydrite
381 at room temperature was determined as 36.6e-6 1/°C by Evans (1979). Zhang et al. (2007) use a
382 thermal expansion coefficient of Monfared et al. (2011) who determine the solid thermal
383 expansion coefficient of Opalinus Claystone as 30e-6 1/°C.
384 Zhang et al. (2007) modelled experiments on Opalinus Clay with bulk ("wet") linear thermal
385 expansion coefficients of 15e-6 1/°C by using a fluid volumetric thermal expansion coefficient of
386 340e-6 1/°C and a solid linear thermal expansion coefficient of 1.5e-6 1/°C.

387 As indicated above, for the low porosity Zechstein and Limburg formations we assume that the
388 bulk volumetric thermal expansion coefficient equals to the solid volumetric thermal expansion
389 coefficient of the minerals as suggested by Palciauskas and Domenico (1982). The thermal
390 expansion coefficients of liquid-saturated sandstones are not much different from dry sandstones
391 (Somerton, 1992). Also, no large differences were found between the thermal expansion
392 coefficients of Quartz and Sandstones. Therefore, we also assume that bulk thermal expansion
393 coefficient is equal to solid thermal expansion coefficient for the Slochteren sandstone formation.
394 For the base case scenario, we use a bulk volumetric thermal expansion coefficient of $30 \times 10^{-6} \text{ 1/}^\circ\text{C}$
395 for all three layers with a potential variability in the Slochteren sandstone between 20×10^{-6} and
396 $40 \times 10^{-6} \text{ 1/}^\circ\text{C}$. Even though Halite has a volumetric thermal expansion coefficient of $120 \times 10^{-6} \text{ 1/}^\circ\text{C}$,
397 the Zechstein is a very complex formation including additionally anhydrite ($\alpha_v \sim 37 \times 10^{-6} \text{ 1/}^\circ\text{C}$),
398 carbonates ($\alpha_v \sim 12\text{-}36 \times 10^{-6} \text{ 1/}^\circ\text{C}$) and claystones ($\alpha_v \sim 30 \times 10^{-6} \text{ 1/}^\circ\text{C}$). Additionally, a much lower
399 volumetric thermal expansion coefficient was determined for Zechstein rock samples in
400 laboratory experiments ($\alpha_v \sim 43\text{-}54 \times 10^{-6} \text{ 1/}^\circ\text{C}$) and most other rock forming minerals have much
401 lower thermal expansion coefficients in the order of $3 \times 10^{-6} \text{ 1/}^\circ\text{C}$. Since the solid thermal expansion
402 coefficient of clay is similar to that of Quartz, we also use $30 \times 10^{-6} \text{ 1/}^\circ\text{C}$ for the Limburg formation.

403 *Solid density*

404 Quartz has a solid density of 2650 kg/m^3 (Blake, 2008). This value is used for the Rotliegend
405 reservoir layer in the base case model. Daniilidis et al. (2016) consider a density range of 2500-
406 2700 kg/m^3 . We therefore adopt this range as approximate lower and upper bounds.
407 The solid density of halite is 2170 kg/m^3 . Daniilidis et al. (2016) use the same value for the
408 Zechstein formation in their model. We therefore use a solid density of 2170 kg/m^3 for the

409 Zechstein layer. The actual solid density of the Zechstein layer may vary significantly (Doddema,
410 2012).

411 The density of clay minerals typically ranges between 2000 and 3000 kg/m³ while many are near
412 2650 kg/m³ (Blake, 2008). We therefore use 2650 kg/m³ as solid density of the Limburg layer.

413 **Fault properties**

414 The fault is modelled as planar discontinuity with finite aperture. Fault asperities and roughness
415 are not considered. In the base case scenario, we assume that the fault has the same properties
416 as the reservoir rock (100 mD permeability and 20% porosity). The fault aperture a is calculated
417 from the permeability k using the cubic law: $a = \sqrt[3]{12k}$. As upper and lower bound we assume 0
418 and 100% porosity and 0 and 10 D permeability.

419 Hunfeld et al. (2017) determined fault friction coefficients of 0.66 for the Basal Zechstein, 0.37 for
420 the Ten Boer claystone, 0.6 for the Rotliegend sandstone, and 0.5 for the Carboniferous. Even
421 though other researchers (Buijze et al., 2017) use different fault friction coefficients for the
422 different units as determined from these laboratory experiments (Hunfeld et al., 2017, 2020) and
423 some fault cohesion between 0 and 3 MPa, we assume a cohesionless fault with a uniform fault
424 friction coefficient of 0.6 that lies approximately between 0.5 and 0.7 due to the inherent
425 uncertainty in these parameters.

426 **Reservoir fluid properties**

427 The reservoir fluid is saline water (brine) with pressure and temperature dependent fluid
428 properties. For the base case model, we use fluid density, viscosity, heat capacity and bulk
429 modulus determined for the Groß Schönebeck (GrSk) site (NaCl, KCl, and CaCl₂ molality of 1.815,
430 0.043 and 1.399, respectively) using the code BrineProp_0.7.3.1 (Francke et al., 2013). A 5 mol

431 NaCl/kg H₂O solution, which has a similar salinity as the Groß Schönebeck fluid, was assumed for
432 the volumetric thermal expansion coefficient and the thermal conductivity. Viscosity and thermal
433 expansion coefficient have the largest temperature/pressure dependence. Additionally,
434 considering the salinity is important for all other fluid properties. For the viscosity, a temperature
435 and pressure dependent look-up table is used. Bulk modulus, density, thermal conductivity and
436 heat capacity are almost not affected by pressure and temperature changes. Thus, constant
437 values are assumed here. We do not explicitly implement fluid thermal expansion coefficients in
438 the model, as these values are integrated into the pore thermal expansion coefficient.
439 For the sensitivity analysis we use the pressure and temperature dependent water properties
440 from REFPROP (Lemmon et al., 2018) and typical variations within the expected salinity range of
441 0-400 g/l and pressure and temperature range.

442 **3.2. Delft sandstone reservoir models**

443 This section describes the hydrothermal reservoir properties above the Permian salt in the
444 Netherlands. The considered reservoir formation is the Delft Sandstone Member. This massive
445 sandstone sequence is overlain by the Rodenrijs Member, an organic rich claystone, which is used
446 as the top layer in this model. The Alblasserdam Member (flood-plain deposits) is used as the
447 bottom layer in this model.

448 **3.2.1. Model geometry and boundary conditions**

449 We simplify the geology to a conceptual model consisting of a horizontal claystone layer
450 (Rodenrijs Member) as top seal, a horizontal sandstone layer (Delft Sandstone) as reservoir unit
451 and a horizontal claystone layer (Alblasserdam Member) lower bound. Again, all layers are
452 intersected by a single inclined fault and no fault offset is assumed. We note that, in contrast to

453 our model, faults in nature usually share some degree of offset. Data from the Groningen gas
454 field show that most mapped faults have an offset of up to 100 m, occasionally even more than
455 200 m (Buijze, 2020). However, with offset faults, there are discontinuities in the material
456 properties on both sides of the fault, leading to peaks in shear and normal stresses at the
457 intersections between formation and fault (e.g. Van Wees et al., 2017). Numerical simulations
458 amplify these stress peaks due to simplified geometry (e.g. sharp material boundaries, no
459 damage zone, planar fault) and mechanics (homogeneous linear elastic medium). In addition, the
460 mesh size can influence the amplitude of the observed peaks (Jansen and Meulenbroek, 2022).
461 We therefore assumed zero-offset faults in our study to avoid these simplifications leading to
462 numerical artefacts in the calculation of the slip tendency. This simplification allows us to analyse
463 the relative impact of certain geological and operational scenarios on the (re)activation potential
464 of faults. However, when interpreting the absolute values of the calculated slip tendencies, it is
465 important to consider these limitations of our model.

466 Hot water production and cold-water injection is also modelled through a typical Dutch
467 geothermal well doublet. Both wells are vertical and intersect the entire Delft sandstone
468 reservoir. They are assumed to be open to flow along the entire well path inside the reservoir
469 formation.

470 The same geometry is used as for the Slochteren model. The top layer was artificially extended to
471 1000 m to avoid boundary effects in the model, thus integrating all overlaying formations as well.
472 The thickness of the Alblasterdam Member varies significantly between <100 m and >1300 m. A
473 thickness of 1000 m is chosen as representative for the bottom layer. The same temperature,
474 pressure and stress gradients as well as heat flow values are used as in the Slochteren Model. The

475 same operational and wellbore data were used in the Delft Sandstone model as in the Slochteren
476 Sandstone model. Variations in other model properties are described below.

477 **3.2.2. Rock matrix, fault and fluid properties**

478 No consistent literature values were found for Rodenrijs, Delft Sandstone and Alblasserdam.

479 Therefore, the values from the Slochteren model were used for Sandstone and Claystone. For the
480 Alblasserdam Member approximately average values between Rodenrijs Member and Delft
481 Sandstone Member were used.

482 Compared to the Slochteren reservoir, the Delft Sandstone Member has a higher permeability.

483 The top and bottom layers have a higher porosity. Thermophysical properties of the Delft
484 Sandstone layer were based on the Slochteren Sandstone model and adapted based on Willems
485 et al. (2020). Rodenrijs properties were based on the claystone properties from the Slochteren
486 model and Alblasserdam properties were based on a mix between sandstone and claystone
487 properties with specific information taken from Willems et al. (2020). For the Delft Sandstone
488 model, the same fault properties as in the Slochteren Sandstone model were used. Due to the
489 lack of reservoir fluid data, we assume pure water as representative reservoir fluid for the Delft
490 Sandstone model.

491 Besides the base case Delft Sandstone model, a small sensitivity analysis is performed for re-
492 injection temperature and well-to-fault distance.

493 **3.3. Dinantian limestone reservoir models**

494 The Dinantian carbonate formation is the deepest formation we consider in our analysis. Here,
495 we simplify the geology to a horizontal Limburg claystone layer as top seal, a horizontal Dinantian
496 limestone layer as reservoir layer and a horizontal Devonian claystone-sandstone layer as bottom

497 seal. Due to the low permeability of the rock matrix we consider three models for geothermal
498 exploitation of the Dinantian limestone: a) wells intersect a high permeability fault (“Dinantian
499 fault model”), b) wells intersect a fault zone (“Dinantian fault damage zone model”), and c)
500 hydraulically fractured parallel horizontal wells are drilled next to the fault representing a multi-
501 stage Enhanced Geothermal System (“Dinantian EGS model”).

502 **3.3.1. Model geometry and boundary conditions**

503 The depth of the Dinantian varies between 2 and 9 km. For the considered Ultra Deep
504 Geothermal development with temperatures $>120^{\circ}\text{C}$ we use a 4.5 km deep Dinantian reservoir
505 top. A thickness of 500 m is assumed. The same thickness is used for the top and bottom layers.
506 Fault geometry and properties are the same as in the Slochteren model. All stress, pressure and
507 temperature initial and boundary conditions are the same as in the Slochteren model adapted for
508 the depth.

509 Operational and wellbore data is the same as in the other two models except that for one
510 scenario, the two deviated wells are 1000 m apart and intersect the fault; and in another
511 scenario two horizontal wells parallel to the minimum horizontal stress direction are 500 m apart
512 and hydraulically connected by 5 hydraulic fractures with a spacing of 200 m. The distance
513 between wells and fault is here 250 m.

514 Three models are setup for the Dinantian reservoir. Due to the low reservoir permeability
515 geothermal exploitation needs to focus on existing fault zones (Scenarios S37 and S38) or
516 stimulated fractures (Scenario S39). Figure 5 and Figure 6 display the geometries of the Dinantian
517 limestone reservoir models.

518

519 **3.3.2. Rock matrix, fault and fluid properties**

520 The description of the Limburg properties can be found in the respective sections on the
521 Slochteren model. The Devonian properties are an approximate average of claystone and
522 sandstone and thus correspond to the Alblasserdam Member as defined above for the Delft
523 model. For the Dinantian, typical values for limestone were used when no specific reservoir
524 information was available.

525 **Geomechanical rock properties**

526 For the Dinantian limestone a Young's modulus of 40 GPa and a Poisson's ratio of 0.2 were used
527 according to the value for the Carboniferous in Lele et al. (2015). According to Schmitt (2015) the
528 solid bulk moduli of Calcite and Dolomite are 73.3 GPa and 94.9 GPa, respectively. Assuming a
529 calcite dominated limestone, we use a value of 80 GPa. The resulting drained bulk modulus and
530 Biot coefficient are 22.2 GPa and 0.72, respectively.

531 **Hydraulic rock properties**

532 The Dinantian is a low porosity and low permeability limestone formation. Similar or even lower
533 values can be expected for the top and bottom layers. Flow is governed by fracture flow.

534 **Thermophysical rock properties**

535 According to Fuchs et al. (2015), Calcite and Dolomite have a thermal conductivity of 3.4 and 5.4
536 W/m/°C, a heat capacity of 820 and 870 J/kg/°C, and a density of 2710 and 2880 kg/m³,
537 respectively. We use values closer to the ones of Calcite. Srinivasan (1955) report similar values of
538 thermal expansion coefficient for calcite and for quartz. Therefore, we use the same value of 30
539 1e-6/°C for the Dinantian limestone and for the Slochteren Sandstone.

540 **Fault and fracture properties**

541 Fracture apertures based on FMI logs in the Dinantian carbonates, were approximately 110 μm
542 (Broothaers et al., 2019; Leverink and Geel, 2019). Assuming this fracture aperture to be
543 equivalent to the hydraulic aperture, the cubic law yields a fracture permeability of 1000 mD.
544 Thus, we use the same fault properties as in the Slochteren model except for a higher fault
545 permeability of 1000 mD, a correspondingly higher aperture of $110\text{e-}6$ m and a higher fault
546 porosity of 100%. The same parameters were used for hydraulic fractures.

547 **Reservoir fluid properties**

548 No fluid information is available for the deep Dinantian limestone formation. We thus use high
549 salinity fluid of the Groß Schönebeck reservoir as formation fluid. This is the same as in the
550 Slochteren model.

551 **4. Results**

552 **4.1. Slochteren sandstone**

553 **4.1.1. Base case model**

554 With the base case model geometry and parameters, the model showed a potential fault failure
555 after 11.45 years of cold-water injection when the maximum slip tendency on the fault reaches
556 the critical value of 0.6 (Figure 7). Figure 8 shows the temperature and pressure contours around
557 the injection well and the slip tendency on the fault plane after 30 years of circulation. The slip
558 tendency values increase systematically when the cold thermal front reaches the fault plane. The
559 pressure perturbation due to the injection process on the other hand, stabilizes relatively quickly
560 and does play only a secondary role in the slip tendency on the fault plane. Figure 9 illustrates the
561 initial and final absolute stresses, thermal stress, pore-pressure and temperature along x-axis and
562 z-axis across the injection well after 30 years of geothermal operation. The figure shows an

563 increased thermal stresses at the formation boundaries. This occurs due to the higher rock
564 stiffness of the top and the bottom layers. It can also be observed from Figure 9 that the
565 maximum pore-pressure increase around the injection well is 3.8 MPa. The temperature around
566 the injection well reaches the injection water temperature i.e. 30°C. Thermal stresses generated
567 due to the temperature change affect the mechanical stress state of the rocks. The combined
568 effect of the thermal, hydraulic and mechanical processes result in an increase in the computed
569 slip tendency along the fault. After 30 years of cold water injection $\sim 0.077 \text{ km}^2$ fault area
570 undergoes failure and the fault plane within the reservoir section experiences a maximum slip
571 tendency of 0.85.

572 **4.1.2. Sensitivity analysis**

573 To understand the impact of the most important reservoir geometries, geological and operational
574 parameters, a sensitivity analysis was performed. The results obtained from the sensitivity
575 analysis cases were only analysed in the reservoir section to ensure the same initial stress state.
576 Figure 10 shows that the parameters that constitute the thermal and mechanical governing
577 equations have the highest impact on the fault failure potential. These parameters included the
578 stress gradients; geo-mechanical reservoir properties like Young's modulus and Poisson's ratio;
579 operational and wellbore data such as the distance between the wells and the fault, re-injection
580 temperature, flow rate; other geological properties like temperature and pressure gradients,
581 thermal expansion coefficient, fault dip, reservoir depth and porosity of the reservoir rock. Many
582 of these parameters also impacted the magnitudes of maximum temperature change along the
583 fault (Figure 11). This indicates a strong correlation between the thermal stresses and the
584 computed slip tendency values as dictated by equation (3). However, such correlation was not

585 observed with the maximum change in pressure values given in Figure 12. Parameters such as
586 pore-pressure differential, permeability, and fluid viscosity did exert only a minor impact on the
587 slip tendency of the fault, indicating how the hydraulic feedback coupling is not significant to
588 determine the fault failure mechanism. A cross examination of Figure 10 and Figure 13 indicates
589 that the cases with higher slip tendencies also resulted in a larger area of the fault with a
590 potential to fail. Even by assuming the same amount of slip for the two cases, a larger area would
591 result in a larger seismic moment and therefore in a higher magnitude of the potential induced
592 event assuming that the slip would be seismic. Figure 14 shows that these cases also failed earlier
593 than the cases with low slip tendency values.

594 One simulation scenario was considered without thermo-elastic effects which resulted in a
595 significant change in the slip tendency on the fault plane. The maximum slip tendency without
596 thermo-elastic effects is only 0.27 instead of 0.85, highlighting the importance of thermal effects
597 on slip tendency in our models. Two special case scenarios were also simulated: (a) a deep low
598 porosity reservoir model and, (b) a shallow high porosity reservoir model. The maximum slip
599 tendencies observed in the reservoir layer in these cases after 30 years of geothermal operation
600 were 0.7 and 0.4 respectively, indicating that deep low porosity reservoirs have a higher fault slip
601 potential compared to shallow high porosity reservoirs.

602 **4.2. Delft sandstone**

603 **4.2.1. Base case model**

604 The Delft sandstone reservoir shows a potential fault failure after 3.95 years of cold-water injection.
605 With 30 years of geothermal operation, the fault plane within the reservoir section experiences a
606 maximum slip tendency of 1 and a fault area of 0.091 km² potentially undergoes failure. The

607 maximum change in the temperature at the fault section within reservoir unit is 54.2°C. As
608 compared to the Slochteren sandstone base case model, the Delft sandstone model experienced
609 a higher slip tendency and a quicker fault failure. This can be attributed to the difference in the
610 geometry of the two models. A smaller reservoir thickness of the Delft reservoir leads to a wider
611 distribution of the thermal front.

612 **4.2.2. Sensitivity analysis**

613 A sensitivity analysis was performed for different re-injection fluid temperatures: (a) 15°C, (b) 30°C
614 (base case) and (c) 45°C. With 15°C re-injection temperature, the rock matrix experiences higher
615 thermal stresses as compared to the base case and thus, fault failure occurs earlier at 3.15 years.
616 The change in temperature at the fault surface after 30 years is 69.6°C with a failure area of 0.10
617 km². The scenario with re-injection water temperature of 45°C, on the other hand, experiences
618 lower thermal stresses as compared to the base case. The fault failure occurs after 6.45 years. The
619 maximum temperature change on the fault plane after 30 years is 38.8°C and the critically stressed
620 fault area is 0.056 km².

621 In another sensitivity analysis scenario, the distance between the injection well and the fault was
622 increased to 500 m. In this case, the fault failure was not observed within the operational period
623 of 30 years. The maximum slip tendency was observed to be 0.51, the maximum temperature
624 change on the fault to be 84.4°C and the maximum pressure change on the fault was 84.1 MPa.

625 **4.3. Dinantian limestone**

626 **4.3.1. Fault-dominated exploitation**

627 In the Dinantian base case model and the Dinantian damage zone model, the injection and
628 production wells intersect the fault. In both the cases fault failure is observed at the beginning of

629 circulation. Figure 15 shows the cross-sections across the injection wells in each case. The injection
630 water flows outwards into the reservoir unit in the base case model, whereas in the damage zone
631 model, the cold injection water flows primarily through the fault damage zone also intersecting the
632 top and bottom units.

633 **4.3.2. Enhanced Geothermal Systems (EGS)**

634 As compared to the fault-dominated exploitation of the Dinantian limestone reservoir, the EGS
635 models shows significantly lower potential of fault failure. The injected water in the EGS models is
636 distributed into the reservoir unit through the hydraulic fractures. As a result, the temperature
637 changes primarily affect the immediate vicinity of the injection well, and have little impact on the
638 stress changes occurring on the fault plane. Figure 16 shows the slip tendency on the fault plane
639 in the EGS models after 30 years of circulation. The EGS system with 500m distance between the
640 injection well and the fault shows no failure potential whereas the EGS model with 250m distance
641 between the injection well and the fault shows failure potential after 28.7 years.

642 **5. Discussion**

643 The study suggests that for the given assumptions and boundary conditions, the changes in the
644 slip tendency of a fault (2D planar discontinuity with zero cohesion) can largely be attributed to
645 thermo-mechanical effects. Once a new equilibrium is reached in a doublet system after a few
646 months, the direct influence of pore pressure on slip tendency remains constant, while the cold-
647 water front will continue to expand around the injection well for as long as the well is in
648 operation. A significant increase in the slip tendency was observed when this low temperature
649 front reached the fault zone. Besides the obvious importance of the stress field and the local fault
650 geometry, rock mechanical properties and operating conditions have a major influence on the

651 induced stress changes and the related fault activation potential triggered by geothermal
652 operations. Thus, careful selection of a suitable target formation and the operational parameters
653 is crucial to minimize the risk of induced seismicity. The most important geological parameters
654 that should be known while selecting the geothermal site are the regional stress gradients,
655 temperature gradient, pressure gradient, geo-mechanical properties of the reservoir layer such as
656 the Young's modulus and Poisson's ratio, thermal expansion coefficient of the formation, fault
657 orientation, reservoir porosity, depth and thickness of the reservoir layer. Lower stress,
658 temperature and pressure gradients, lower reservoir rock stiffness, shallower depth, higher
659 reservoir porosity, larger reservoir thickness, lower thermal expansion coefficient and higher fault
660 dip contribute to a low risk geothermal environment. Besides selecting a low risk geothermal
661 formation, the failure potential can further be minimized by optimizing operational parameters.
662 The key planning and operational parameters to be considered include the distance between the
663 injection well and existing known faults, re-injection temperature and injection flow rate. During
664 the geothermal operations, the most effective measures to reduce the risk of induced seismicity
665 are increasing the re-injection temperature and decreasing the injection rate. The EGS system
666 with optimized well-to-fault distance can be an effective technique for the mitigation of induced
667 seismicity in deeper reservoirs such as Dinantian limestone.

668 In this study we did not consider fault offsets to avoid further complexity in the interpretation of
669 the results and numerical artefacts in the form of stress concentrations on sharp geometrical
670 edges, which are not found in reality, as described before. With a fault offset of less than 200 m
671 (hydraulic connection between reservoir formation on both sides of the fault), the effect would
672 be similar to the results of the sensitivity analysis of the reservoir thickness. Within the 0-200 m

673 range, a larger fault offset would lead to a pressure increase and temperature reduction on the
674 fault, leading to earlier fault slip and increasing slip tendencies. With larger fault offsets, the
675 impermeable Limburg claystone formation on the other side of the fault would prevent flow and
676 convective heat transfer across the fault, leading to higher pressures, but significantly less
677 temperature changes on the fault and thus significantly lower slip tendencies. This case would
678 thus be similar to the impermeable fault scenario.

679 We note again, that although the slip tendency may indicate fault reactivation, it does not tell
680 anything about the seismicity to be expected from this fault failure. Therefore, we performed an
681 additional analysis by applying the rate-and-state friction (RSF) formalism to the same model to
682 get some information about the dynamics of a potential fault slip (Supplementary material S1).

683 The empirical constants describing the frictional properties of the fault in the RSF framework
684 were taken from Hunfeld et al. (2017). The RSF parameters provided in the cited study were
685 determined by direct shear experiments performed on simulated Slochteren Sandstone fault
686 gouges. These experiments did not include fluid injection and did not consider the effect of long-
687 term thermal stressing of the samples. Nevertheless, based on Hunfeld et al. (2017) the
688 Slochteren Sandstone fault gouges show velocity strengthening behaviour in the direct shear
689 experiments, and consequently our RSF model also resulted in slow, stable slip, which might be
690 an indicator for aseismic slip (Guglielmi et al., 2015). Hunfeld et al. (2017) have also indicated that
691 the overlying Zechstein formation shows velocity weakening characteristics. Since in our model
692 the pore pressure and cooling induced stress changes are mainly limited to the fault area
693 overlapping with the reservoir layer (see Fig. 8), we neglected the potentially different friction
694 behaviour of the Zechstein caprock and characterised the entire fault with a single parameter set.

695 This choice is justified by the fact that no significant seismicity (i.e. $M_w > 2$) is observed in the
696 hydrothermal systems of the Netherlands and the velocity strengthening behaviour of the faults
697 in these reservoirs could be one potential reason for this. Nevertheless, faults in the Netherlands
698 may also exhibit velocity weakening behaviour and adapting the RSF parameters in our model
699 accordingly would lead to seismic rather than aseismic slip. A thorough analysis of the frictional
700 behaviour of reactivating faults in the Slochteren Sandstone formation (related to geothermal
701 operation) has to be the subject of future studies based on field observation and site-specific
702 geological models.

703 A limitation of the current model is the lack of validation with field observations from the
704 Netherlands due to the lack of data. No induced seismicity has been observed in the
705 conventional matrix-type geothermal reservoirs in the Netherlands, whereas a previously
706 observed induced seismicity in the Dinantian limestone reservoir indicates the need of a detailed
707 analysis of the geological and operational settings of EGS systems.

708 We note, that we have chosen a simplified approach to include the Zechstein formation in our
709 simulations by modelling it as a homogeneous linear elastic layer without considering secondary
710 creep mechanism. This was done intentionally to avoid further model complexity since this study
711 focuses mainly on the fluid injection induced seismicity inside the respective reservoir layers. In
712 addition, considering the Zechstein formation as a homogeneous viscoelastic layer that consists
713 of pure rock salt would also be a similarly strong assumption. However, it was shown in the case
714 of the Groningen gas field that the presence of the viscoelastic Zechstein caprock can contribute
715 to depletion induced seismic slip (Wassing et al., 2017; Candela et al., 2019).

716 Therefore, the absolute values for slip tendency, failure area, temperature and pressure should

717 be interpreted considering the limitations and assumptions of our model. Nevertheless, the
718 absolute values demonstrate how the calculated slip tendency for this model changes when the
719 input parameters are changed within realistic ranges that apply to the Netherlands.

720 Potential future studies can include site specific model geometries, further refined meshes, a
721 non-linear failure criterion, poro-elastic coupling and a creep constitutive law for the Zechstein
722 salt. It has to be noted that implementing more realistic fault systems (e.g., en echelon
723 segmented) will have a major impact on the individual interplay of key impact factors and
724 resulting slip and induced seismicity patches along the fault.

725 **6. Conclusions**

726 Our results of Dutch geothermal well doublet THM models indicate that thermal effects can play
727 a major role in fault stability, supporting the observations of recent numerical modelling studies
728 (Wassing et al., 2021; Kivi et al., 2022). Cooling induced thermal stresses cause tensile stresses,
729 thereby reducing the magnitude of the resulting compressive stresses. This increases the slip
730 tendency of the fault. Thermal stresses are highly sensitive to geo-mechanical reservoir rock
731 properties e.g. Young's modulus and Poisson's ratio. The higher the rock stiffness, the higher the
732 chances of failure during cold fluid injection. Within the range of investigated geometries, the
733 Slochteren sandstone exhibits a more stable fault configuration when characterized by a higher
734 fault dip and a fault strike that is oriented at a greater angle relative to the SHmax direction.
735 According to the sensitivity analysis, a significant variation in stress gradients across different
736 principal directions corresponds to elevated shear stresses, which increases the potential for fault
737 failure. Among the thermal properties, bulk thermal expansion coefficient has the most
738 significant effect on fault stability. Well-to-fault distance, re-injection temperature, and injection

739 flow rate are key parameters that can influence the seismic risk. Therefore, it is essential to
740 carefully consider these parameters when planning a geothermal system. In the case of typical
741 Slochteren deep geothermal systems, hydraulic parameters and fluid properties such as rock
742 permeability, fluid viscosity and fluid density have minor impact on fault stability within their
743 respective investigated ranges.

744 **Acknowledgements**

745 The authors are grateful for the financial support provided by the “Kennis Effecten Mijnbouw”
746 (KEM)-programme through the project “Risk of seismicity due to cooling effects in geothermal
747 systems – KEM-15”, and input from Staatstoezicht op de Mijnen (SodM, Dutch State Supervision
748 on Mines), particularly Richard Bakker, Niels Grobbe and Annemarie Muntendam-Bos. We also
749 thank FUGRO for providing the expertise on the geological background. We kindly acknowledge
750 the financial support of the Helmholtz Association’s Initiative and Networking Fund for the
751 Helmholtz Young Investigator Group ARES (contract number VH-NG-1516).

752 **Authors’ contributions:**

753 BM set up and carried out all simulations presented in the manuscript. HH gathered and
754 compiled the reservoir and fluid data and supervised the study, MC helped set up and
755 troubleshoot the simulation input files, GH supported the mesh refinement and time step
756 optimization and performed the RSF analysis in the supplementary material, AZ supervised the
757 study. All authors collaborated on the writing.

758 **Competing Interests statement:**

759 The authors declare no competing interests.

760 **References**

761 Bekesi E., Struijk M., Bonte D., Veldkamp H., Limberger J., Fokker P. A., Vrijlandt M., and Wees J. D
762 (2020): An updated geothermal model of the Dutch subsurface based on inversion of
763 temperature data. *Geothermics* 88, p.101880.

764 Buijze, L., van den Bogert, P.A.J., Wassing, B.B.T., Orlic, B., ten Veen, J. (2017): Fault reactivation
765 mechanisms and dynamic rupture modelling of depletion-induced seismic events in a Rotliegend
766 gas reservoir. *Netherlands Journal of Geosciences – Geologie en Mijnbouw* 96(5):131-148.
767 <https://doi.org/10.1017/njg.2017.27>

768 Buijze, A. J. L. (2020). Numerical and experimental simulation of fault reactivation and earthquake
769 rupture applied to induced seismicity in the Groningen gas field (Doctoral dissertation, Utrecht
770 University).

771 Blackwell D, Steele J. (1989): Heat flow and geothermal potential of Kansas. *Biul Kans Geol Surv.*
772 226:267–95.

773 Blake G.R. (2008) Particle density. In: Chesworth W. (eds) *Encyclopedia of Soil Science.*
774 *Encyclopedia of Earth Sciences Series.* Springer, Dordrecht. [https://doi.org/10.1007/978-1-4020-](https://doi.org/10.1007/978-1-4020-3995-9_406)
775 [3995-9_406](https://doi.org/10.1007/978-1-4020-3995-9_406)

776 Blöcher, M.G., Zimmermann, G., Moeck, I., Brandt, W., Hassanzadegan, A., Magri, F. (2010): 3D
777 numerical modelling of hydrothermal processes during the lifetime of a deep geothermal
778 reservoir. *Geofluids* 10:406-421. <https://doi.org/10.1111/j.1468-8123.2010.00284.x>

779 Blöcher, G., Cacace, M., Jacquy, A. B., Zang, A., Heidbach, O., Hofmann, H., Kluge, C.,
780 Zimmermann, G. (2018): Evaluating Micro-Seismic Events Triggered by Reservoir Operations at
781 the Geothermal Site of Groß Schönebeck (Germany). - *Rock Mechanics and Rock Engineering*, 51,
782 10, 3265-3279. <https://doi.org/10.1007/s00603-018-1521-2>

783 Bonte D., Wees J. D. V., and Verweij H. J. Subsurface temperature of the onshore Netherlands:
784 new temperature data set and modelling". *Netherlands Journal of Geosciences / Geologie en*
785 *Mijnbouw* 91-4 (2012), pp.491- 515.

786 Broothaers, M., Bos, S., Lagrou, D., Harcouët-Menou, V. and Laenen, B. (2019): Lower
787 Carboniferous limestone reservoir in northern Belgium: structural insights from the Balmatt
788 project in Mol. *European Geothermal Congress Proceedings*, The Hague.

789 Buijze L., Lonneke v. B., Cremer H., Paap B., Veldkamp H., Wassing B. T., Wees J. D., Yperen G. C.
790 N., Jaarsma B., Heege J. H. (2020): Review of induced seismicity in geothermal systems worldwide
791 and implications for geothermal systems in the Netherlands-CORRI- GENDUM. *Netherlands*
792 *Journal of Geosciences* 99, e10.

793 Cacace M. and Blöcher G. (2015): MeshIt-a software for three dimensional volumetric meshing of
794 complex faulted reservoirs. *Environmental Earth Sciences* 74, pp.5191-5209.
795 <https://doi.org/10.1007/s12665-015-4537-x>.

796 Cacace, M., Jacquy, A.B. (2017): Flexible parallel implicit modelling of coupled thermal

797 hydraulic mechanical processes in fractured rocks. *Solid Earth*, 8.5.

798 Cacace, M., Hofmann, H., & Shapiro, S. A. (2021). Projecting seismicity induced by complex
799 alterations of underground stresses with applications to geothermal systems. *Scientific Reports*,
800 11(1), 23560.

801 De Jager, J. (2007): Geological development. *Geology of the Netherlands* Edited by Th.E. Wong,
802 D.A.J. Batjes & J. de Jager. Royal Netherlands Academy of Arts and Sciences, 2007: 5–26

803 De Simone, S., Vilarrasa, V., Carrera, J., Alcolea, A., Meier, P. (2013): Thermal coupling may control
804 mechanical stability of geothermal reservoirs during cold water injection. *Physics and Chemistry*
805 *of the Earth* 64:117-126. <https://doi.org/10.1016/j.pce.2013.01.001>

806 Delage, P. (2013): On the thermal impact on the excavation damaged zone around deep
807 radioactive waste disposal. *International Journal of Rock Mechanics and Geotechnical*
808 *Engineering* 5:179-190. <http://dx.doi.org/10.1016/j.jrmge.2013.04.002>

809 Destress (2021): <http://www.destress-h2020.eu/en/demonstration-sites/middenmeer>

810 Daniilidis, A., Doddema, L., Herber, R. (2016): Risk assessment of the Groningen geothermal
811 potential: From seismic to reservoir uncertainty using a discrete parameter analysis. *Geothermics*
812 64:271-288. <http://dx.doi.org/10.1016/j.geothermics.2016.06.014>

813 Dinoloket (2021): <https://www.dinoloket.nl/en/subsurface-models>

814 Doddema, L. (2012). The influence of reservoir heterogeneities on geothermal doublet
815 performance. Master Thesis. University of Groningen.

816 Duin, E.J.T., Doornenbal, J.C., Rijkers, R.H.B., Verbeek, J.W., Wong, T.E. (2006): Subsurface
817 structure of the Netherlands – results of recent onshore and offshore mapping. *Netherlands*
818 *Journal of Geosciences – Geologie en Minjbouw* 85(4):245-276.
819 <https://doi.org/10.1017/S0016774600023064>

820 Evans Jr., H.T. (1979): The thermal expansion of Anhydrite to 1000°C. *Phys. Chem. Minerals* 4:77-
821 82. <https://doi.org/10.1007/BF00308361>

822 Falzone, A.J., Stacey, F.D. (1982): Measurements of thermal expansions of small mineral crystals.
823 *Phys. Chem. Minerals* 8:212-217.

824 Francke, H, Kraume, M., Saadat, M. (2013): Thermal-hydraulic measurements and modelling of
825 the brine circuit in a geothermal well. *Environmental Earth Sciences* 70:3481-3495.
826 <http://dx.doi.org/10.1007/s12665-013-2612-8>

827 Foulger, G.R., Wilson, M.P., Gluyas, J.G., Julian, B.R., Davies, R.J. (2018): Global review of human-
828 induced earthquakes. *Earth-Science Reviews* 178:438-514.
829 <https://doi.org/10.1016/j.earscirev.2017.07.008>

830 Fuchs, S., Balling, S. Förster, A. (2015): Calculation of thermal conductivity, thermal diffusivity and

831 specific heat capacity of sedimentary rocks using petrophysical well logs, *Geophysical Journal*
832 *International* 203(3):1977–2000, <https://doi.org/10.1093/gji/ggv403>

833 Ghabezloo S, Sulem J. (2008): Stress dependent thermal pressurization of a fluid-saturated rock.
834 *Rock Mech Rock Eng* 2008;42:1–24. <https://doi.org/10.1007/s00603-008-0165-z>

835 Ghassemi, A., Tarasovs, S., Cheng, A.h.-D. (2007): A 3-D study of the effects of thermomechanical
836 loads on fracture slip in enhanced geothermal reservoirs. *International Journal of Rock Mechanics*
837 *and Mining Sciences* 44(8):1132-1148. <https://doi.org/10.1016/j.ijrmms.2007.07.016>

838 Griffith, J. (1936): Thermal expansion of typical American rock. *Iowa State College of Agriculture*
839 *and Mechanics Arts. Iowa Engineering Experiments* 35 (19), 24.

840 Guglielmi, Y., Cappa, F., Avouac, J. P., Henry, P., & Elsworth, D. (2015). Seismicity triggered by fluid
841 injection–induced aseismic slip. *Science*, 348(6240), 1224-1226.

842 Guises, R., Embry, J.-M., Barton, C. (2015): Dynamic Geomechanical Modelling to Assess and
843 Minimize the Risk for Fault Slip during Reservoir Depletion of the Groningen Field. Baker Hughes
844 project report for NAM, project reference: NAM0001, Revision No. 1, June 2015.

845 Hassanzadegan, A., Blöcher, G., Zimmermann, G., Milsch, H. (2012): Thermoporoelastic
846 properties of Flechtinger sandstone. *International Journal of Rock Mechanics and Mining*
847 *Sciences* 49:94-104. <https://doi.org/10.1016/j.ijrmms.2011.11.002>

848 Huenges, E., Ellis, J., Welter, S., Westaway, R., Min, K. B., Genter, A., ... & Marti, M. (2020).
849 Demonstration of soft stimulation treatments in geothermal reservoirs. In *Proceedings of the*
850 *world geothermal congress (Vol. 1)*.

851 Hunfeld, L.B., Niemeijer, A.R., Spiers, C.J. (2017): Frictional properties of simulated fault gouges
852 from the seismogenic Groningen gas field under in situ P-T-Chemical conditions. *Journal of*
853 *Geophysical Research Solid Earth* 122(11):8969-8989. <https://doi.org/10.1002/2017JB014876>

854 Hunfeld, L.B., Chen, J., Hol, S., Niemeijer, A.R., Spiers, C.J. (2020): Healing behaviour of simulated
855 fault gouges from the Groningen gas field and implications for induced fault reactivation. *Journal*
856 *of Geophysical Research Solid Earth* 125(7):e2019JB018790.
857 <https://doi.org/10.1029/2019JB018790>

858 Hurter, S., Schellschmidt, R. (2003): Atlas of geothermal resources in Europe. *Geothermics* 32(4-
859 6):779-787. [https://doi.org/10.1016/S0375-6505\(03\)00070-1](https://doi.org/10.1016/S0375-6505(03)00070-1)

860 Hutka, G. A., Cacace, M., Hofmann, H., Zang, A., Wang, L., & Ji, Y. (2023). Numerical investigation
861 of the effect of fluid pressurization rate on laboratory-scale injection-induced fault slip. *Scientific*
862 *Reports*, 13(1), 4437.

863 Jacquy , A. B., Cacace, M. (2017): GOLEM, a MOOSE-based application. url:
864 <https://doi.org/10.5281/zenodo.999401>.

865 Jaeger, J.C., Cook, N.G.W., Zimmerman, R.W. (2007): *Fundamentals of rock mechanics*. Fourth

866 Edition. Blackwell Publishing, pp. 475.

867 Jansen, J. D., & Meulenbroek, B. (2022). Induced aseismic slip and the onset of seismicity in
868 displaced faults. *Netherlands Journal of Geosciences*, 101, e13.

869 Kansy, A. (2007): Einfluss des Biot-Parameters auf das hydraulische Verhalten von Steinsalz unter
870 der Berücksichtigung des Porendrucks. TU Clausthal, Fakultät für Energie- und
871 Wirtschaftswissenschaften, Dissertation. Clausthal.

872 Kivi, I.R., Pujades, E., Rutqvist, J., Vilarrasa, V. (2022): Cooling-induced reactivation of distant
873 faults during long-term geothermal energy production in hot sedimentary aquifers. *Scientific*
874 *Reports* 12(2065). <https://doi.org/10.1038/s41598-022-06067-0>

875 Lele, S.P., Garzon, J.L., Hsu, S.-Y., DeDontney, N.L., Searles, K.H., Sanz, P.F. (2015): Groningen 2015
876 Geomechanical analysis. NAM report, November 2015.

877 Lemmon, E.W., Bell, I.H., Huber, M.L., McLinden, M.O. (2018). NIST Standard Reference Database
878 23: Reference Fluid Thermodynamic and Transport Properties-REFPROP, Version 10.0, National
879 Institute of Standards and Technology, Standard Reference Data Program, Gaithersburg.

880 Van Leverink, D., Geel, K. (2019): Fracture characterization of the Dinantian carbonates in the
881 Dutch subsurface. Report by SCAN, November 2019.

882 Van Wees, J. D., Fokker, P. A., Van Thienen-Visser, K., Wassing, B. B., Osinga, S., Orlic, B., ... &
883 Pluymaekers, M. (2017). Geomechanical models for induced seismicity in the Netherlands:
884 Inferences from simplified analytical, finite element and rupture model approaches. *Netherlands*
885 *Journal of Geosciences*, 96(5), s183-s202.

886 McTigue DF (1986): Thermoelastic response of fluid-saturated porous rock. *J Geophys Res*91(B9):
887 9533–9542. <https://doi.org/10.1029/JB091iB09p09533>

888 Mechelse, E. (2017): The in-situ stress field in the Netherlands: Regional trends, local deviations
889 and an analysis of the stress regimes in the northeast of the Netherlands. Master Thesis, TU
890 Delft.

891 Mijnlief, H.F. (2020): Introduction to the geothermal play type and reservoir geology of the
892 Netherlands. *Netherlands Journal of Geosciences* 99(e2). <https://doi.org/10.1017/njg.2020.2>

893 Mohammed, A.K.A. (2020): A review: controls on sandstone permeability during burial and its
894 measurements comparison—example, Permian Rotliegend Sandstone. *Model. Earth Syst.*
895 *Environ.* 6, 591–603. <https://doi.org/10.1007/s40808-019-00704-w>

896 Monfared, M., Sulem, J., Delage, P. (2011): A Laboratory Investigation on Thermal Properties of
897 the Opalinus Claystone. *Rock Mech Rock Eng* 44, 735. [https://doi.org/10.1007/s00603-011-0171-](https://doi.org/10.1007/s00603-011-0171-4)
898 4.

899 Moore, J., McLennan, J., Allis, R., Pankow, K., Simmons, S., Podgorney, R., ... & Rickard, W. (2019,
900 February). The Utah Frontier Observatory for Research in Geothermal Energy (FORGE): an

901 international laboratory for enhanced geothermal system technology development. In 44th
902 Workshop on Geothermal Reservoir Engineering (pp. 11-13). Stanford University.

903 Morris A., Ferrill D. A., and Henderson D. B. (1996): Slip-tendency analysis and fault reactivation.
904 *Geology* 24, pp.275-278.

905 Norbeck, J., Latimer, T., Gradl, C., Agarwal, S., Dadi, S., Eddy, E., ... & Woitt, M. (2023). A review of
906 drilling, completion, and stimulation of a horizontal geothermal well system in North-Central
907 Nevada. In Proceedings of the 48th Workshop on Geothermal Reservoir Engineering, Stanford
908 University, Stanford, CA, February 6-8 2023, SGP-TR-224.

909 Palciauskas V. V., Domenico P. A. (1982): Characterization of drained and undrained response of
910 thermally loaded repository rocks. <https://doi.org/10.1029/WR018i002p00281>

911 Permann C. J., Gaston D. R., Andres D., Carlsen R. W., Kong F., Lindsay A. D., Miller J. M.,
912 Peterson J. W., Slaughter A. E., Stogner R. H., and Martineau R.C. (2020): MOOSE: Enabling
913 massively parallel multiphysics simulation. *SoftwareX* 11, p.100430.

914 Pijnenburg, R.P.J., Verberne, B.A., Hangx, S.J.T., Spiers, C.J. (2019): Inelastic deformation of the
915 Slochteren Sandstone: Stress-Strain Relations and Implications for Induced Seismicity in the
916 Groningen Gas Field. *Journal of Geophysical Research Solid Earth* 124(5):5254-5282.
917 <https://doi.org/10.1029/2019JB017366>

918 Plevová, E., Vaculiková, L., Kozusníková, A., Danek, T., Pleva, M., Ritz, M., Martynková, G.S. (2011):
919 Thermal study of sandstones from different Czech localities. *J Therm Anal Calorim* 103:835-843.
920 <https://doi.org/10.1007/s10973-010-1129-6>.

921 Ramsay J. G. and Lisle R. J. (2000): Applications of continuum mechanics in structural geology.
922 *Techniques of modern structural geology*. Vol.3.

923 Richter A. (2019): The Top10 Geothermal Countries 2019 {based on installed generation capacity
924 (MWe)}. Think GeoEnergy-Geothermal Energy News. Jan. 27, 2020. url:
925 [https://www.thinkgeoenergy.com/the-top-10-geothermal-countries-2019-based-on-installed-](https://www.thinkgeoenergy.com/the-top-10-geothermal-countries-2019-based-on-installed-generation-capacity-mwe/)
926 [generation-capacity-mwe/](https://www.thinkgeoenergy.com/the-top-10-geothermal-countries-2019-based-on-installed-generation-capacity-mwe/).

927 Schmitt, D.R. (2015): 11.03 - Geophysical Properties of the Near Surface Earth: Seismic
928 Properties, Editor Gerald Schubert, *Treatise on Geophysics (Second Edition)*, Elsevier, pp. 43-87,
929 ISBN 9780444538031, <https://doi.org/10.1016/B978-0-444-53802-4.00190-1>.

930 Skinner, B.J. (1966): Thermal expansion. *Geol. Soc. Am. Mem.* 97:75-96.

931 Slizowski, J., Nagy, S., Burliga, S., Serbin, K., Polanski, K. (2015): Laboratory investigations of
932 geotechnical properties of rock salt in Polish salt deposits. Mechanical behavior of salt VIII :
933 Proceedings of the Conference on Mechanical Behavior of Salt, SALTMECH VIII : Rapid City, USA,
934 26–28 May 2015 / eds. Lance Roberts, Kirby Mellegard, Frank Hansen. — Boca Raton, [etc.] : CRC
935 Press Taylor & Francis Group, cop. 2015. — ISBN: 978-1-138-02840-1 ; e-ISBN: 978-1-315-67885-
936 6. — p. 33–38.

937 Somerton, W.H. (1992): Thermal properties and temperature related behaviour of rock/fluid
938 systems. Elsevier, New York.

939 Srinivasan, R. (1955): The thermal expansion of calcite from room temperature up to 400°C. Proc.
940 Indian Acad. Sci. 42, 81–85. <https://doi.org/10.1007/BF03053495>.

941 TNO (2015): Integrated pressure information system for the onshore and offshore Netherlands.
942 Final report. 83 pages.

943 TNO-GSN (2021a): Zechstein Group. Stratigraphic Nomenclature of the Netherlands, TNO –
944 Geological Survey of the Netherlands. Accessed on 28-02-2021 from
945 <http://www.dinoloket.nl/en/stratigraphic-nomenclature/zechstein-group>.

946 Urquhart, A., Bauer, S. (2015): Experimental determination of single-crystal halite thermal
947 conductivity, diffusivity and specific heat from –75 °C to 300 °C. International Journal of Rock
948 Mechanics and Mining Sciences 78:350-352. <https://doi.org/10.1016/j.ijrmms.2015.04.007>.

949 Van Eijs, R.M.H.E. (2015), Neotectonic Stresses in the Permian Slochteren Formation of the
950 Groningen Field. NAM report EP201510210531.

951 Veen J. T., Gessel S. F., and Dulk M. (2012): Thin-and thick-skinned salt tectonics in the
952 Netherlands; A quantitative approach. *Geologie en Mijnbouw* 91, pp.447-464.

953 Veldkamp, J.G., Goldberg, T.V., Bressers, P.M.M.C., Wilschut, F. (2016): Corrosion in Dutch
954 geothermal systems. TNO report R10160, 15 March 2016, p. 105.

955 Verweij, J., Simmelink, H., Underschultz, J., & Witmans, N. (2012): Pressure and fluid dynamic
956 characterisation of the Dutch subsurface. *Netherlands Journal of Geosciences - Geologie En*
957 *Mijnbouw*, 91(4), 465-490. <https://doi.org/10.1017/S0016774600000342>.

958 Vörös, R., Baisch, S. (2022): Induced seismicity and seismic risk management – a showcase from
959 the Californië geothermal field (the Netherlands). *Netherlands Journal of Geosciences* 101(e15).
960 <https://doi.org/10.1017/njg.2022.12>

961 Wang, Y., Khait, M., Voskov, D., Saeid, S., Bruhn, D. (2019): Benchmark test and sensitivity analysis
962 for Geothermal Applications in the Netherlands. Proceedings of the 44th Workshop on
963 Geothermal Reservoir Engineering, Stanford University, Stanford, California, February 11-13,
964 SGP-TR-214.

965 Waples, D.W., Waples, J.S. (2014): A Review and Evaluation of Specific Heat Capacities of Rocks,
966 Minerals, and Subsurface Fluids. Part 1: Minerals and Nonporous Rocks. *Natural Resources*
967 *Research* 13(2):97-122. <https://doi.org/1520-7439/04/0600-0097/1>.

968 Wassing, B. B. T., Buijze, L., Ter Heege, J. H., Orlic, B., & Osinga, S. (2017, June). The impact of
969 viscoelastic caprock on fault reactivation and fault rupture in producing gas fields. In ARMA US
970 Rock Mechanics/Geomechanics Symposium (pp. ARMA-2017). ARMA.

971 Wassing, B. B. T., Candela, T., Osinga, S., Peters, E., Buijze, L., Fokker, P. A., & Van Wees, J. D.

972 (2021). Time-dependent seismic footprint of thermal loading for geothermal activities in
973 fractured carbonate reservoirs. *Frontiers in Earth Science*, 9, 685841.

974 Willems, C., Vondrak, A., Mijnlief, H., Donselaar, M., & Van Kempen, B. (2020): Geology of the
975 Upper Jurassic to Lower Cretaceous geothermal aquifers in the West Netherlands Basin – an
976 overview. *Netherlands Journal of Geosciences*, 99, E1. doi:10.1017/njg.2020.1.

977 Willems, C.J.L., Nick, H.M., Weltje, G.J., Bruhn, D.F. (2017): An evaluation of interferences in heat
978 production from low enthalpy geothermal doublet systems. *Energy* 135:500-512.
979 <https://doi.org/10.1016/j.energy.2017.06.129>.

980 Zang, A., Wagner, C.F., Dresen, G. (1996): Acoustic emission, microstructure, and damage model
981 of dry and wet sandstone stressed to failure. *Journal of Geophysical Research Solid Earth*
982 101(B8):17507-17521. <https://doi.org/10.1029/96JB01189>.

983 Zhang, C.-L., Rothfuchs, T., Jockwer, N., Komischke, M. (2007): Thermal Effects on the Opalius
984 Clay. Final Report. GRS – 224, ISBN 978-3-931995-98-0.
985 https://www.grs.de/sites/default/files/pdf/grs-224_0.pdf.

986 Zhang, D., Jeannin, L., Hevin G., Egermann, P., Potier, L., Skoczylas, F. (2018): Is salt a poro-
987 mechanical material? 52nd US Rock Mechanics / Geomechanics Symposium, Seattle,
988 Washington, USA, 17-20 June 2018. ARMA 18-0423.

989 Zimmerman, R.W. (2000): Coupling in poroelasticity and thermoelasticity. *Int J RockMech Min Sci*
990 37(1–2):79–87. <https://doi.org/10.1016/j.ijrmms.2011.11.002>.

991 Zoback, M.D. (2007): *Reservoir Geomechanics: Earth Stress and Rock Mechanics Applied to*
992 *Exploration, Production and Wellbore Stability*. Cambridge University Press.

993

994 **Tables**

995 Table 1: Mechanical, thermal and hydraulic properties of geological units and the fault in the
 996 Slochteren Sandstone base case model.

Model property	Zechstein (rock salt)	Rotliegend (sandstone)	Limburg (claystone)	Fault
Young's modulus (GPa)	30	15	40	15
Poisson's ratio (-)	0.3	0.2	0.2	0.2
Solid bulk modulus (GPa)	30	40	50	40
Drained bulk modulus (GPa)	25	8.33	22.2	8.33
Biot coefficient (-)	0.17	0.86	0.56	0.86
Friction coefficient (-)	-	-	-	0.6
Cohesion (MPa)	-	-	-	0
Solid thermal conductivity (W/m/°C)	4.5	3.5	2.0	3.5
Solid heat capacity (J/kg/°C)	925	830	860	830
Volumetric bulk thermal expansion coefficient (1e-6/°C)	30	30	30	30
Solid density (kg/m ³)	2170	2650	2650	2650
Hor. permeability (mD)	0.001	100	0.001	100
Hor./vert. permeability (-)	1	2	1	1
Porosity (%)	1	20	1	100

997

998

999 Table 2: Fluid properties of the Slochteren sandstone, Delft sandstone and Dinantian limestone
 1000 models. The viscosity for the Slochteren and Dinantian models is a function of pressure and
 1001 temperature derived from the data from the Groß Schönebeck Rotliegend reservoir fluid. In the
 1002 Delft models a pressure and temperature dependent viscosity function for pure water was used.

Fluid property	Slochteren sandstone model	Delft sandstone model	Dinantian limestone model
Density (kg/m ³)	1154	1154	1154
Viscosity (mPas)	$f(P/T)_{GrSk}$	$f(P/T)_{H_2O}$	$f(P/T)_{GrSk}$
Specific heat capacity (J/kg/°C)	3240	4125	3240
Thermal conductivity (W/m/°C)	0.625	0.65	0.625
Bulk modulus (GPa)	3.4	2.35	3.4

1003

1004

1005 Table 3: Geometrical and wellbore properties of the Slochteren Sandstone model (base case
 1006 scenario).

Model property	Zechstein (rock salt)	Rotliegend (sandstone)	Limburg (claystone)
Unit top (m)	2000	2200	2400
Unit thickness (m)	1000	200	1000
Fault strike	N130°E		
Fault dip (° from horizontal)	80		
Fault dip direction	NE		
Well length (m)	-	200	-
Well diameter (m)	-	0.05	-
Well permeability (m ²)	-	3.12e-4	-
Well porosity (-)	-	1	-

1007

1008

1009 Table 4: Slochteren sandstone, Delft sandstone and Dinantian limestone base case model
 1010 boundary conditions.

Parameter	Value	Boundary condition
Temperature gradient	31°C/km + 10°C	Constant temperature at top and bottom boundary
Pore-pressure gradient	11 MPa/km	Constant pressure gradient on all four vertical boundaries
Vertical stress gradient	23 MPa/km	Constant stress in z direction on top boundary and no displacement in z direction on bottom boundary
Maximum horizontal stress gradient	15 MPa/km	constant displacement in y-direction on front boundary and no displacement in y-direction on back boundary
Minimum horizontal stress gradient	14 MPa/km	constant displacement in x-direction on left boundary and no displacement in x-direction on right boundary
Maximum horizontal stress direction	N160°E	Model boundaries aligned with maximum horizontal stress direction by rotation
Injection rate	70 L/s	Constant injection rate applied to the middle point of the injection well (only during dynamic simulation, not applied to steady state)
Production rate	70 L/s	Constant production rate applied to the middle point of the production well (only during dynamic simulation, not applied to steady state)
Injection temperature	30°C	Constant temperature applied to the middle point of the injection well (only during dynamic simulation, not applied to steady state)

1011

1012

1013 Table 5: Modelling scenarios for the Slochteren sandstone, Delft sandstone and Dinantian
 1014 limestone sensitivity analysis.

Category	Case ID	Changed parameter	Changed values
	S1	Base case scenario	-
Geometry	S2a,b	Depth of reservoir top	1500 m, 3000 m
	S3a,b	Reservoir thickness	100 m, 250 m
	S4	Fault strike	N150°E
	S5a,b,c	Fault dip	60°, 70°, 85°
Geomechanical properties of reservoir	S6a,b	Young's modulus	3 GPa, 30 GPa
	S7a,b	Poisson's ratio	0.1, 0.25
	S8a,b	Biot's coefficient	0.5, 0.97
Hydraulic properties of reservoir	S9a,b	Hor. permeability	50 mD, 350 mD
	S10a,b	Hor./vert. permeability ratio	1, 10
	S11a,b	Porosity	10%, 30%
Thermophysical properties of reservoir	S12a,b	Thermal conductivity	3 W/m/°C, 7.7 W/m/°C
	S13a,b	Heat capacity	650 J/kg/°C, 1050 J/kg/°C
	S14a,b	Bulk thermal expansion coefficient	20e-6 1/°C, 40e-6 1/°C
Fault properties	S15a,b	Fault permeability, porosity	0 D, 0%; 10 D, 100%
Temperature, pressure, stress gradients	S16a,b	Geothermal gradient	20°C/km + 10°C, 40°C/km + 10°C
	S17a,b	Pressure gradient	10 MPa/km, 12 MPa/km
	S18a,b	Vertical stress gradient	21 MPa/km, 23 MPa/km
	S19a,b	Maximum horizontal stress gradient	15 MPa/km, 23 MPa/km
	S20a,b	Minimum horizontal stress gradient	13 MPa/km, 23 MPa/km
	S21a,b	Maximum horizontal stress direction	N150°E, N170°E
Reservoir fluid parameters	S22a,b	Density	980 kg/m ³ , 1200 kg/m ³
	S23a,b	Viscosity	0.3 mPas, 1.5 mPas
	S24a,b	Specific heat capacity	3200 J/kg/°C, 4200 J/kg/°C
	S25a,b	Thermal conductivity	0.6 W/m/K, 0.7 W/m/K
	S26a,b	Bulk modulus	2 GPa, 4 GPa
Operational and wellbore data	S27a,b	Well spacing	500 m, 1500 m
	S28a,b	Re-injection temperature	15°C, 45°C
	S29a,b	Flow rate	30 l/s, 100 l/s
	S30a,b,c	Well to fault distance	0m, 500m, 1000m
Thermoelastic effect	S31	Thermal expansion coefficient	0

Special scenarios	S32	Deep low porosity reservoir	D=3000 m, H=100 m, k=100 mD, T=10 Dm, kh/kv=10, $\phi=10\%$, $\alpha=0.5$, E=30 GPa, $\nu=0.1$, q=40 l/s
	S33	Shallow high porosity reservoir	D=1500 m, H=250 m, k=200 mD, T=50 Dm, kh/kv=1, $\phi=30\%$, $\alpha=0.97$, E=3 GPa, $\nu=0.25$, q=100 l/s
Delft Sandstone model	S34	Base case scenario	-
	S35a,b	Re-injection temperature	15°C, 45°C
	S36a	Well-to-fault distance	500m
Dinantian Limestone model	S37	Base case fault model	-
	S38	Damage zone model	50m fault damage zone
	S39a,b	EGS model	Wells 250m, 500m from fault

1015

1016

1017 Table 6: Mechanical, thermal and hydraulic properties of geological units and the fault in the
 1018 Delft Sandstone base case model.

Model property	Rodenrijs Member (claystone)	Delft Sandstone Member	Albalasserdam Member (sst/clst)	Fault
Young's modulus (GPa)	40	15	25	15
Poisson's ratio (-)	0.2	0.2	0.2	0.2
Solid bulk modulus (GPa)	50	60	45	60
Drained bulk modulus (GPa)	22.2	8.33	13.9	8.33
Biot coefficient (-)	0.56	0.86	0.69	0.86
Friction coefficient (-)	-	-	-	0.6
Cohesion (MPa)	-	-	-	0
Solid thermal conductivity (W/m/°C)	2.0	4.5	2.5	4.5
Solid heat capacity (J/kg/°C)	950	730	860	730
Volumetric bulk thermal expansion coefficient (1e-6/°C)	30	30	30	30
Solid density (kg/m ³)	2650	2650	2650	2650
Hor. permeability (mD)	1	1000	1	100
Hor./vert. permeability (-)	1	2	1	1
Porosity (%)	10	20	10	20

1019

1020

1021 Table 7: Mechanical, thermal and hydraulic properties of geological units and the fault/fractures
 1022 in the Dinantian limestone base case model.

Model property	Limburg (claystone)	Dnantian (limestone)	Devonian (clst/sst)	Fault/fractures
Young's modulus (GPa)	40	40	25	40
Poisson's ratio (-)	0.2	0.2	0.2	0.2
Solid bulk modulus (GPa)	50	80	45	80
Drained bulk modulus (GPa)	22.2	22.2	13.9	22.2
Biot coefficient (-)	0.56	0.72	0.69	0.69
Friction coefficient (-)	-	-	-	0.6
Cohesion (MPa)	-	-	-	0
Solid thermal conductivity (W/m/°C)	2.0	3.5	2.5	3.5
Solid heat capacity (J/kg/°C)	860	830	860	830
Volumetric bulk thermal expansion coefficient (1e-6/°C)	30	30	30	30
Solid density (kg/m ³)	2650	2750	2650	2750
Hor. permeability (mD)	0.001	1	0.001	1000
Hor./vert. permeability (-)	1	1	1	1
Porosity (%)	1	2	1	100

1023

1024

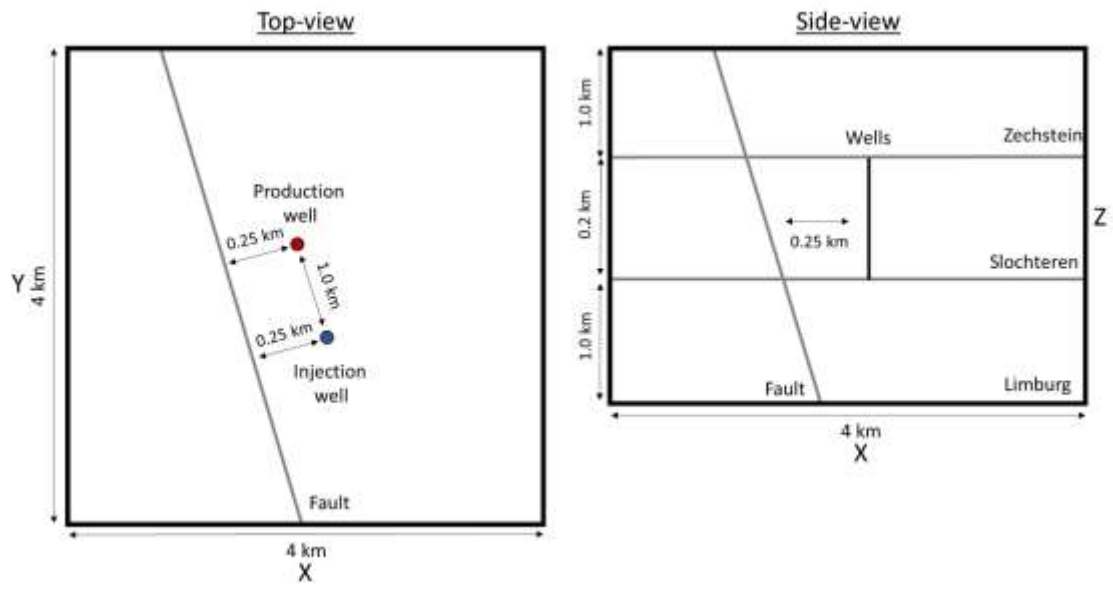
1025 Table 8: Comparison of Slochteren, Delft and Dinantian EGS models.

	Slochteren	Delft	Dinantian EGS
Max ST on fault (in reservoir unit)	0.85	1.0	0.61
Max temperature change on fault (°C)	53.6	54.2	0.89
Max pressure change on fault (MPa)	0.70	0.16	4.7
Area of fault with ST > μ (km ²)	0.077	0.09	0.0013
Time until ST > μ (Years)	11.45	3.95	28.7

1026

1027

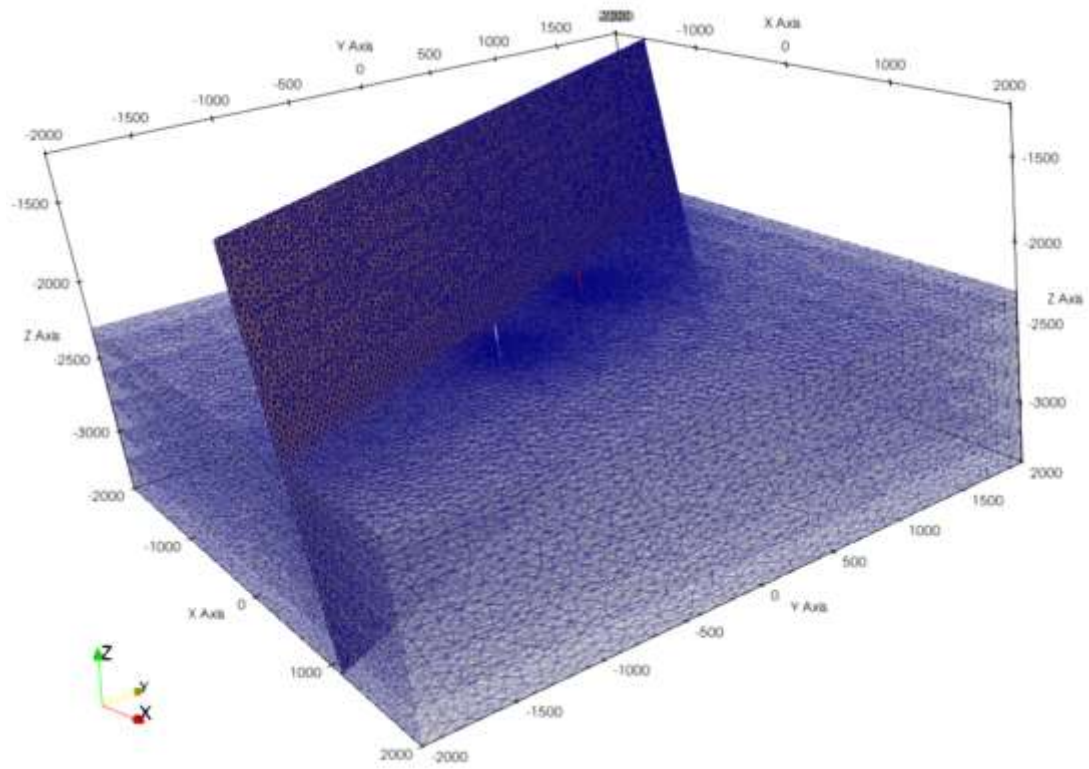
1028 **Figures**



1029

1030 Figure 1: Top view (top left) and side view (top right) for the Slochteren base case model (not
1031 to scale).

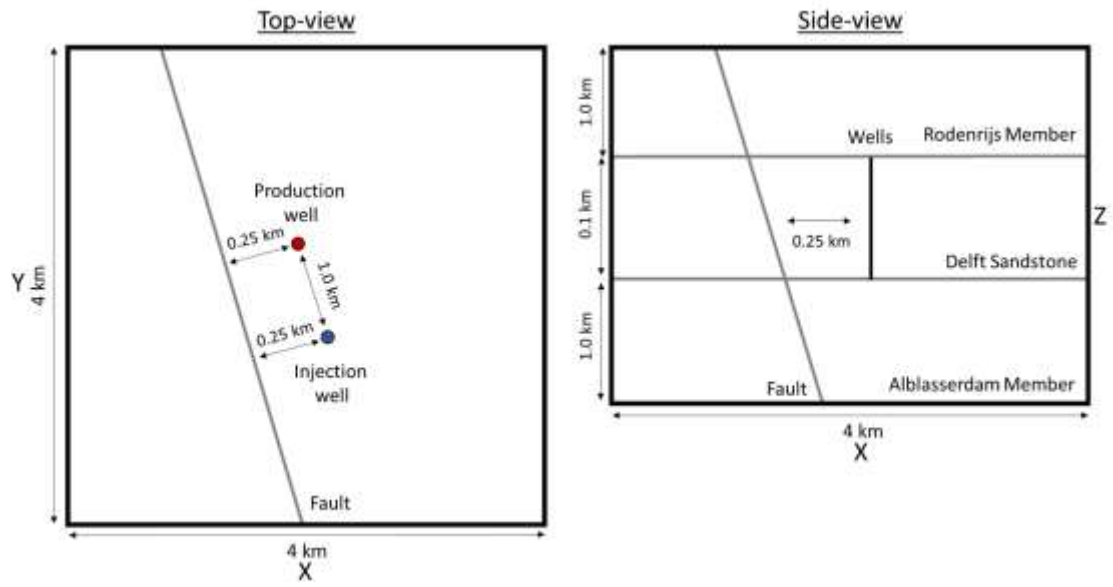
1032



1033

1034 Figure 2: 3D view of the Slochteren base case mesh. Mesh refinement is applied around the
 1035 injection and production wells and in the fault plane within the reservoir unit.

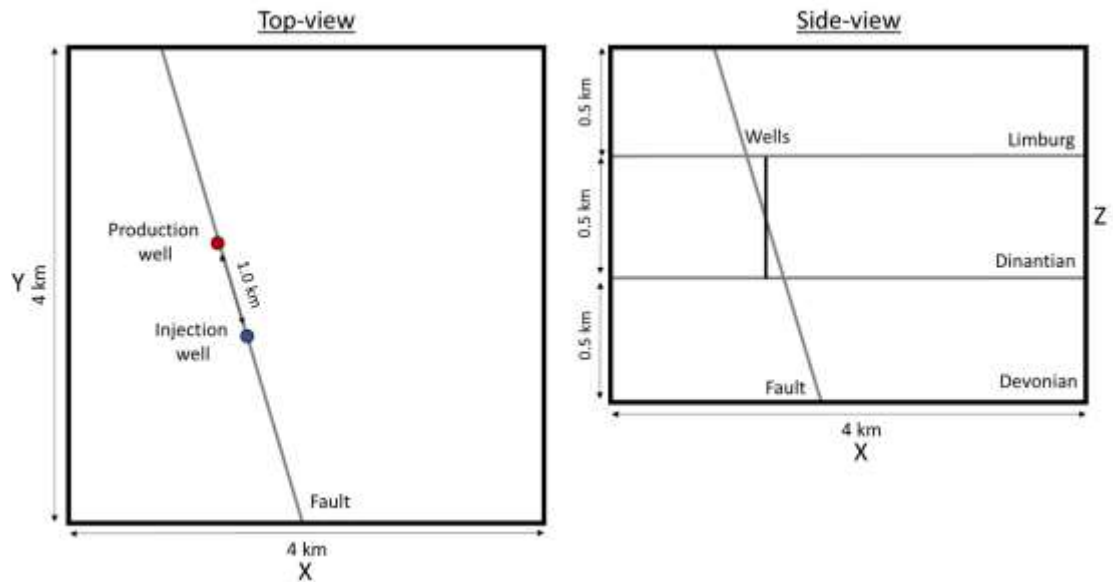
1036



1037

1038 Figure 3: Top (left) and side (right) view of the Delft sandstone model (not to scale).

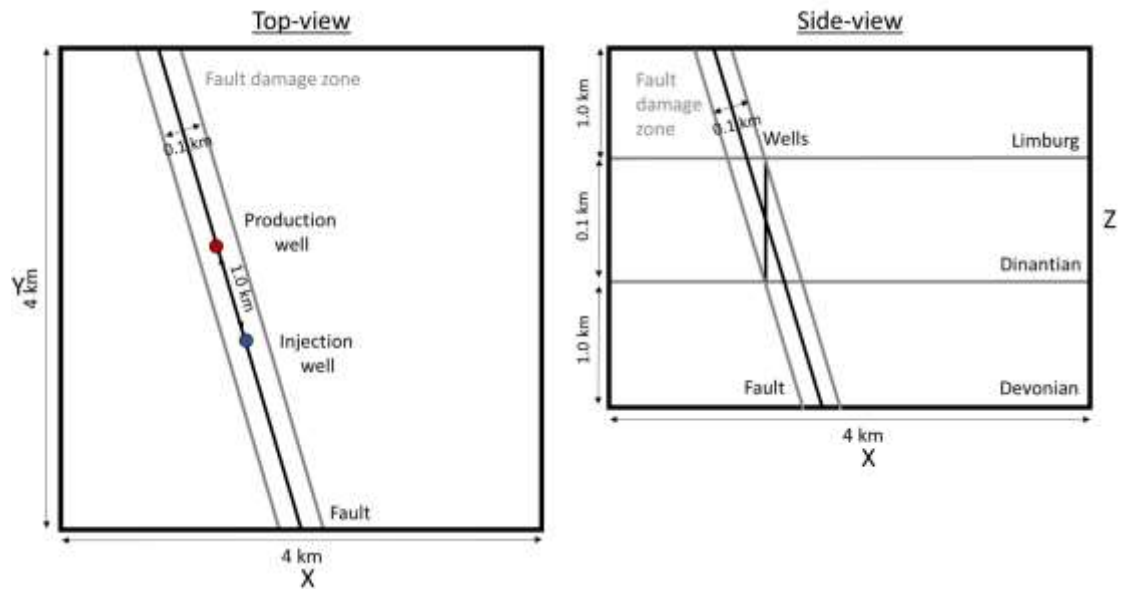
1039



1040

1041 Figure 4: Top (left) and side (right) view of the Dinantian limestone fault model (not to scale).

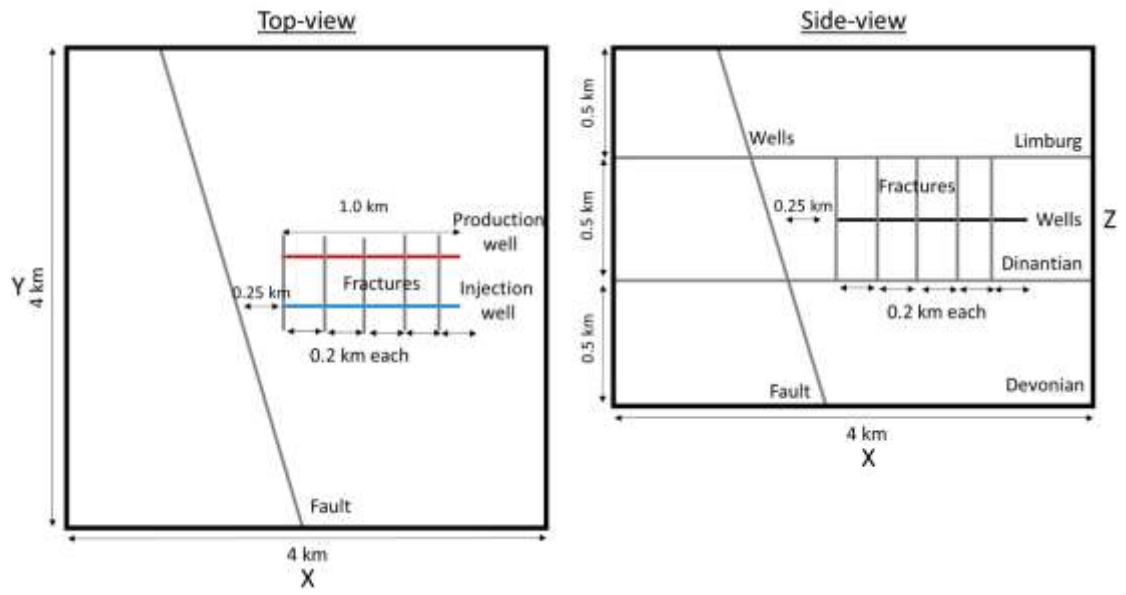
1042



1043

1044 Figure 5: Top (left) and side (right) view of the Dinantian fault damage zone model (not to scale).

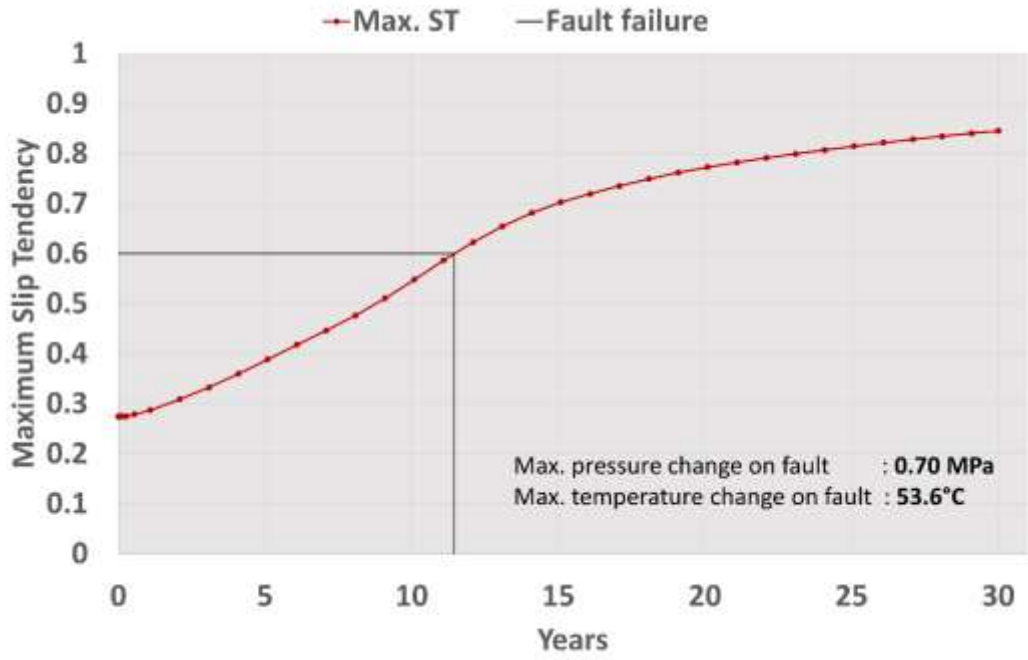
1045



1046

1047 Figure 6: Top (left) and side (right) view of the Dinantian EGS model (not to scale).

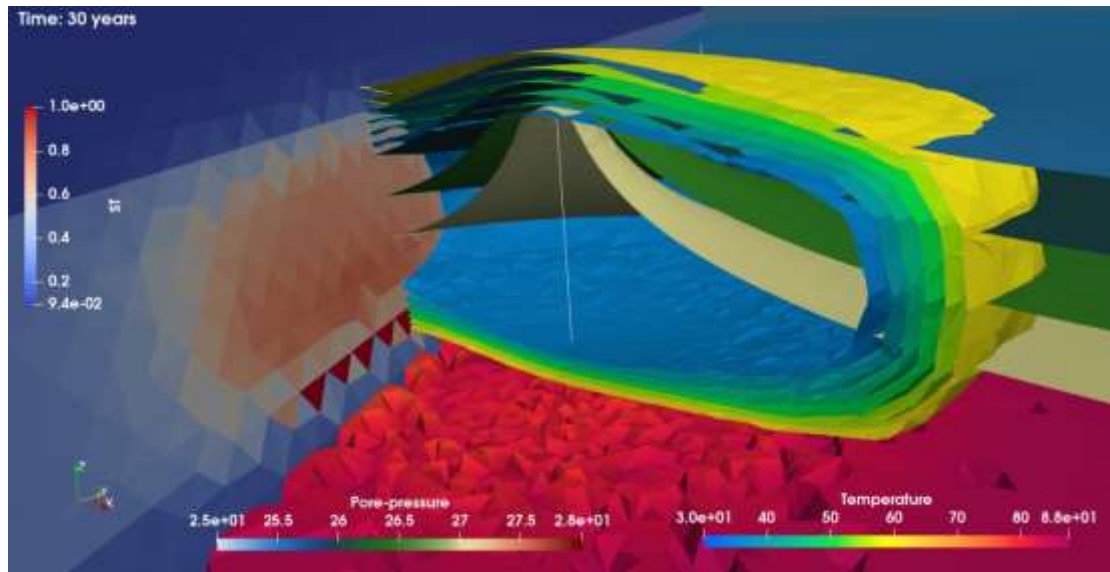
1048



1049

1050 Figure 7: Maximum slip tendency on the fault and fault failure within the reservoir unit of the
 1051 Slochteren base case model.

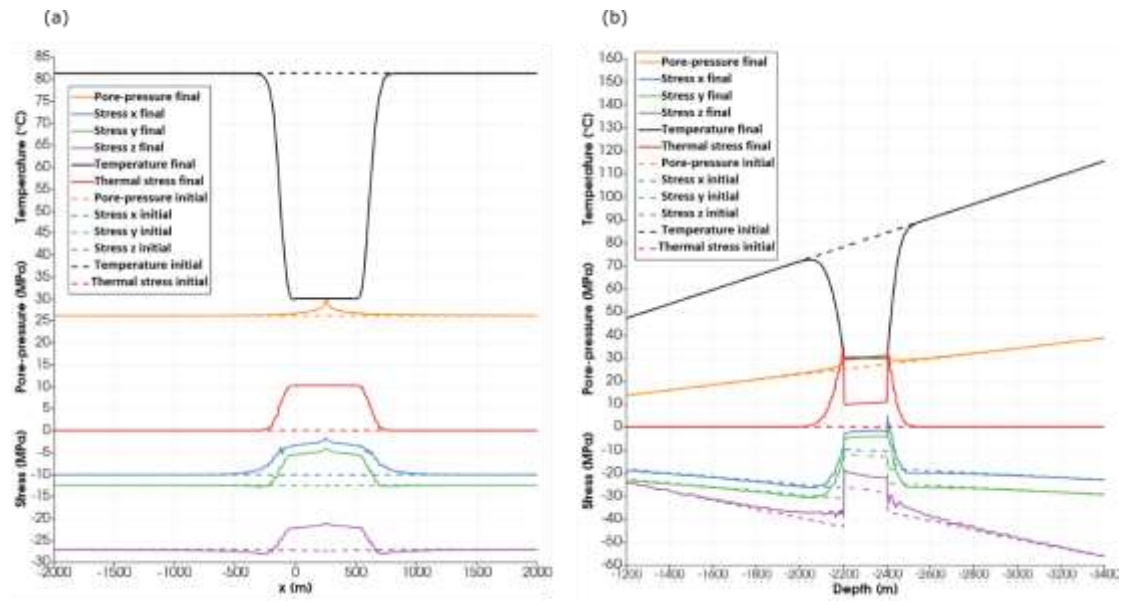
1052



1053

1054 Figure 8: Temperature contours (in °C), pressure contours (in MPa), and slip tendency (unitless)
 1055 on the fault in the Slochteren base case model after 30 years of circulation.

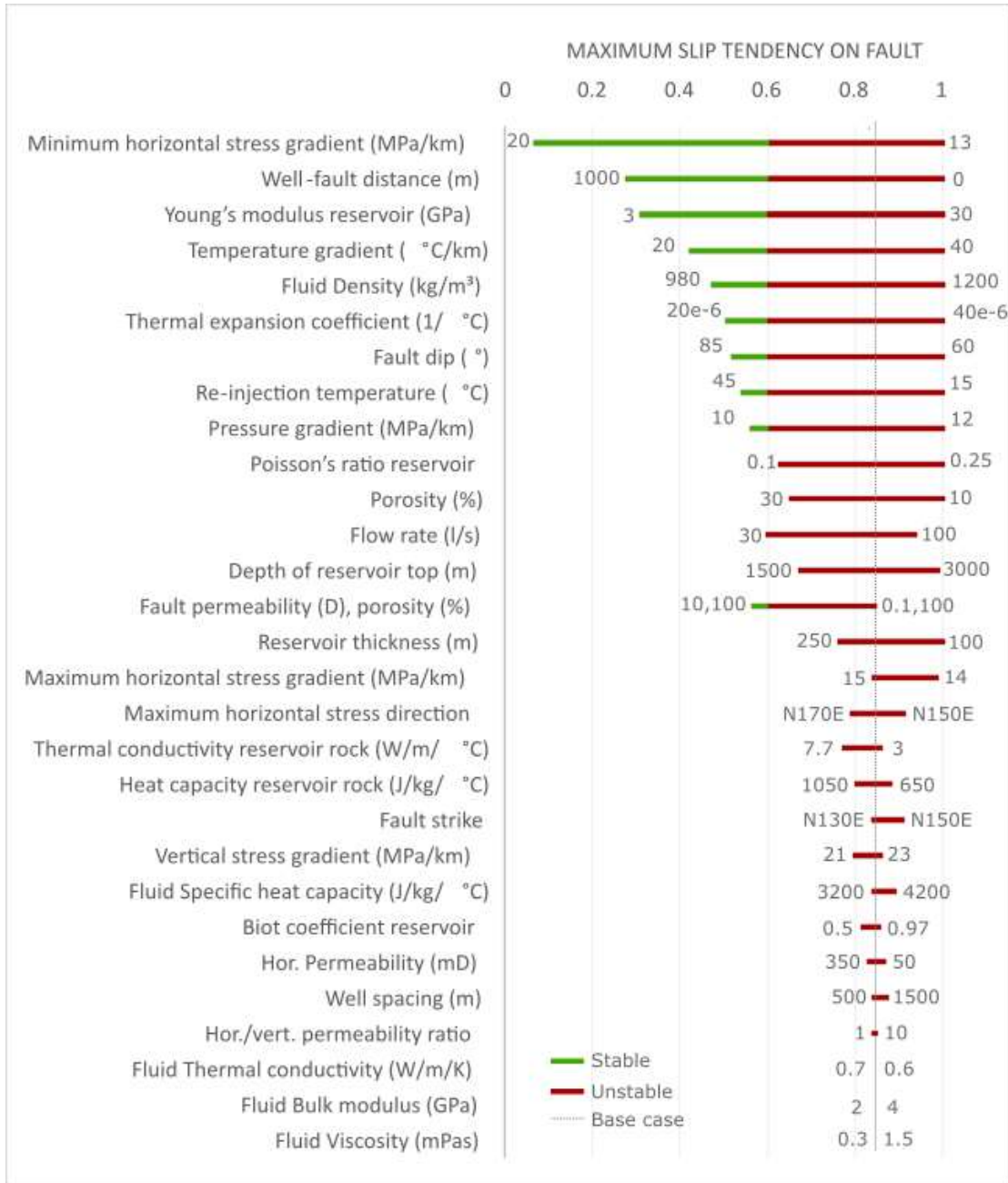
1056



1057

1058 Figure 9: Temperature, pore-pressure and effective stresses (compression is negative) across
 1059 the injection well (a) along x-axis and (b) along z-axis, initial (dash) and after 30 years (solid) of
 1060 circulation in the Slochteren base case model.

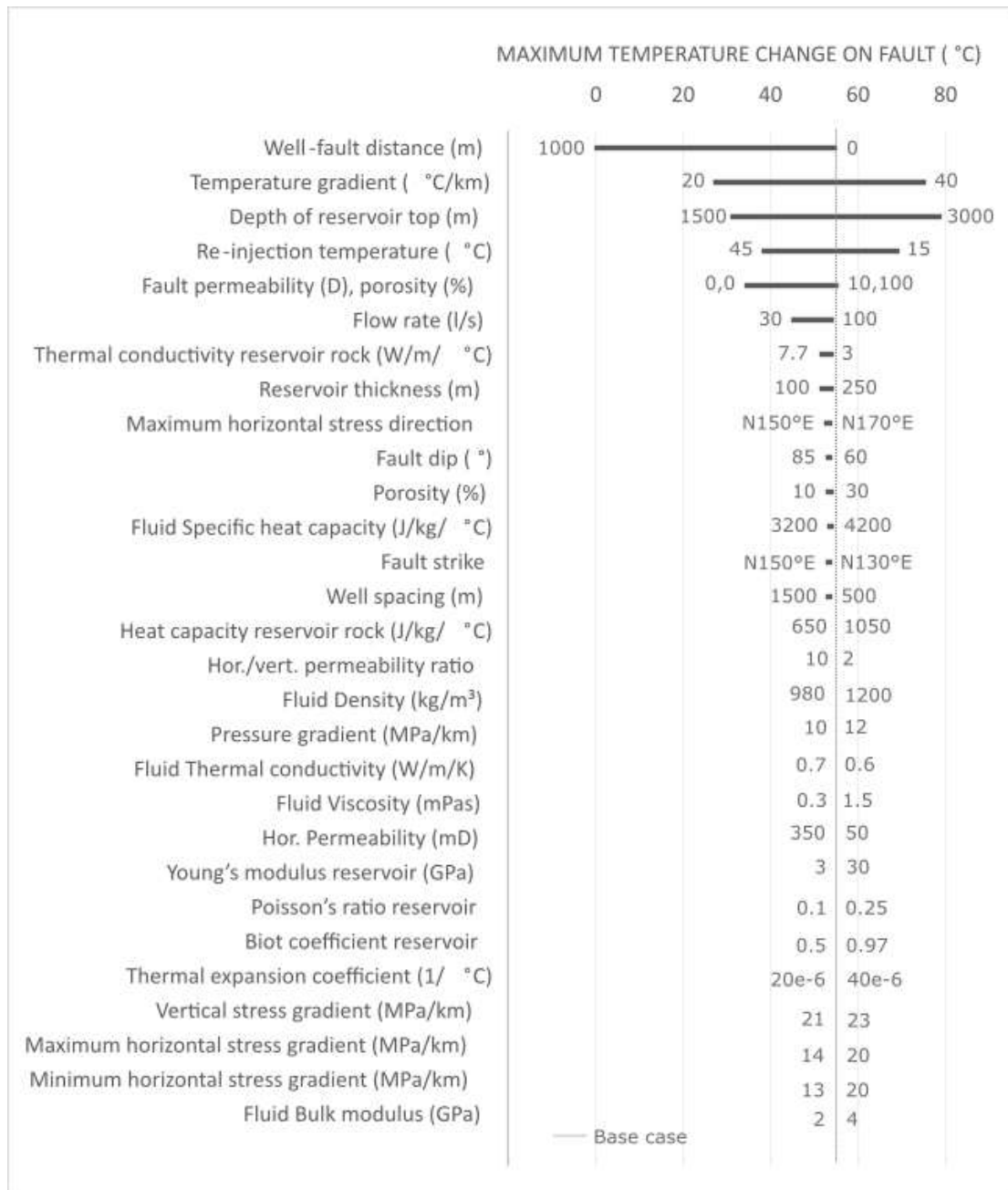
1061



1062

1063 Figure 10: Results of the sensitivity analysis for the fault within the reservoir unit: Maximum slip
 1064 tendency after 30 years of circulation in the Slochteren models.

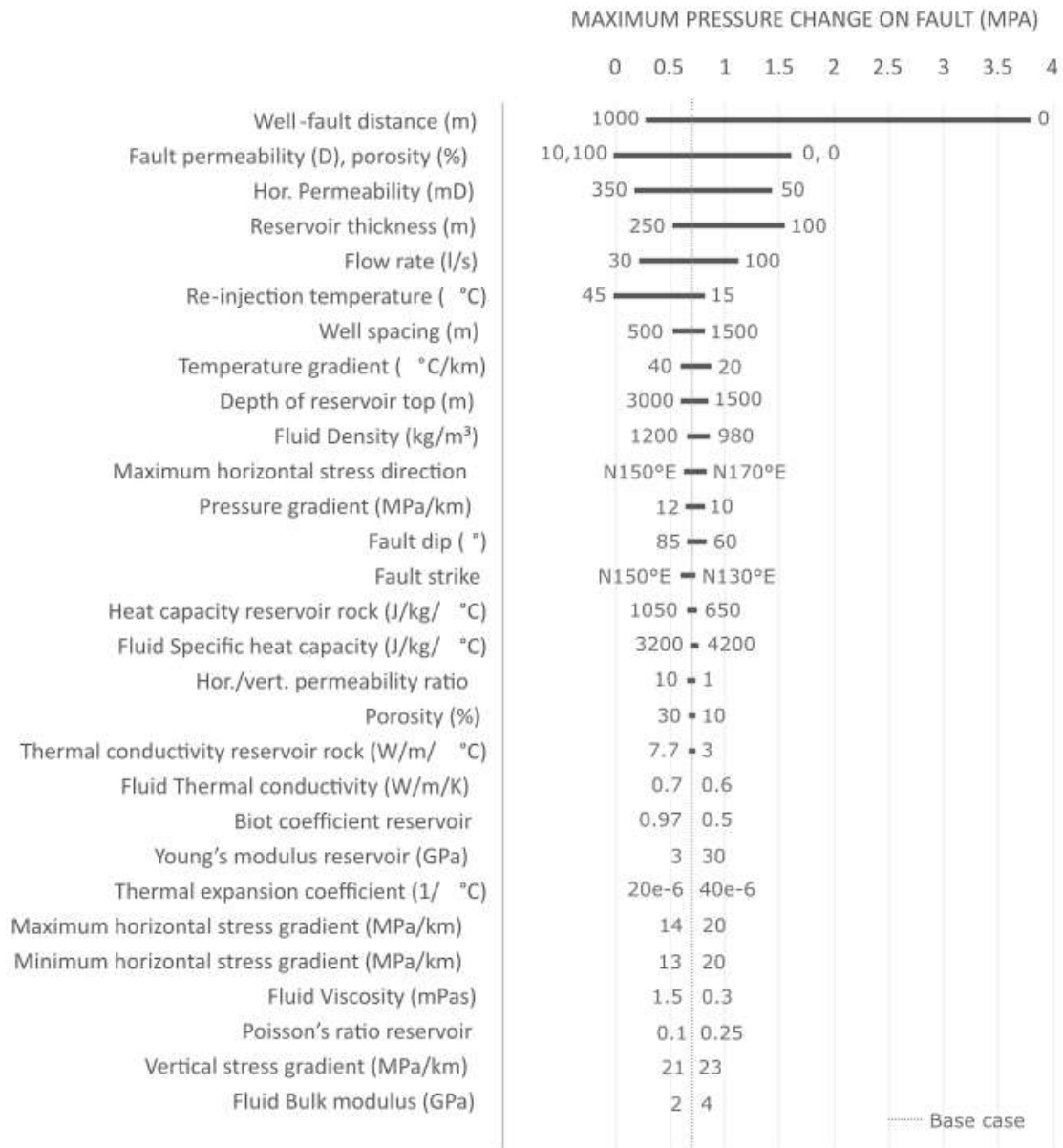
1065



1066

1067 Figure 11: Results of the sensitivity analysis for the fault within the reservoir unit: Maximum
 1068 temperature change after 30 years of circulation in the Slochteren models.

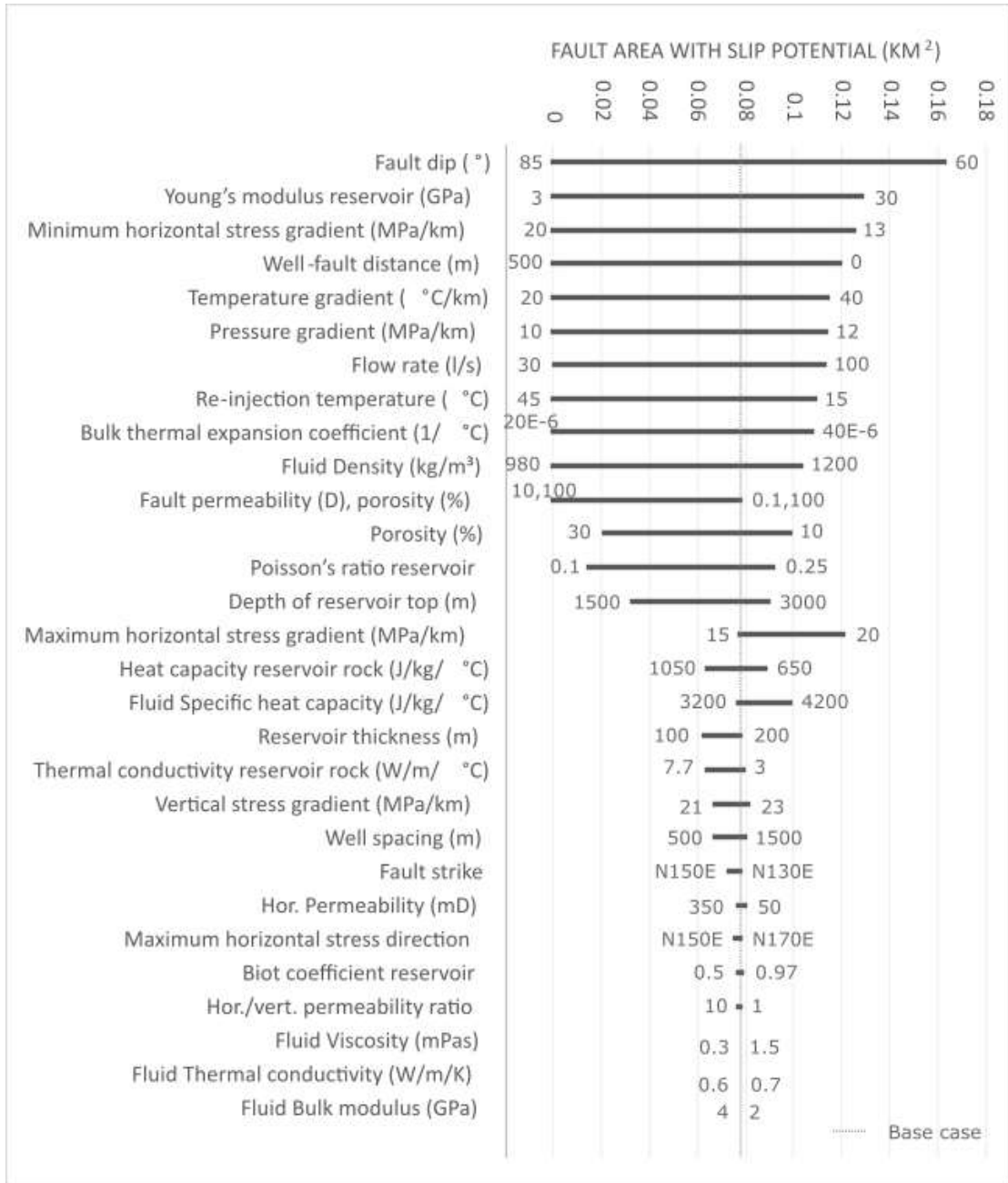
1069



1070

1071 Figure 12: Results of the sensitivity analysis for the fault within the reservoir unit: Maximum
 1072 pore-pressure change after 30 years of circulation in the Slochteren models.

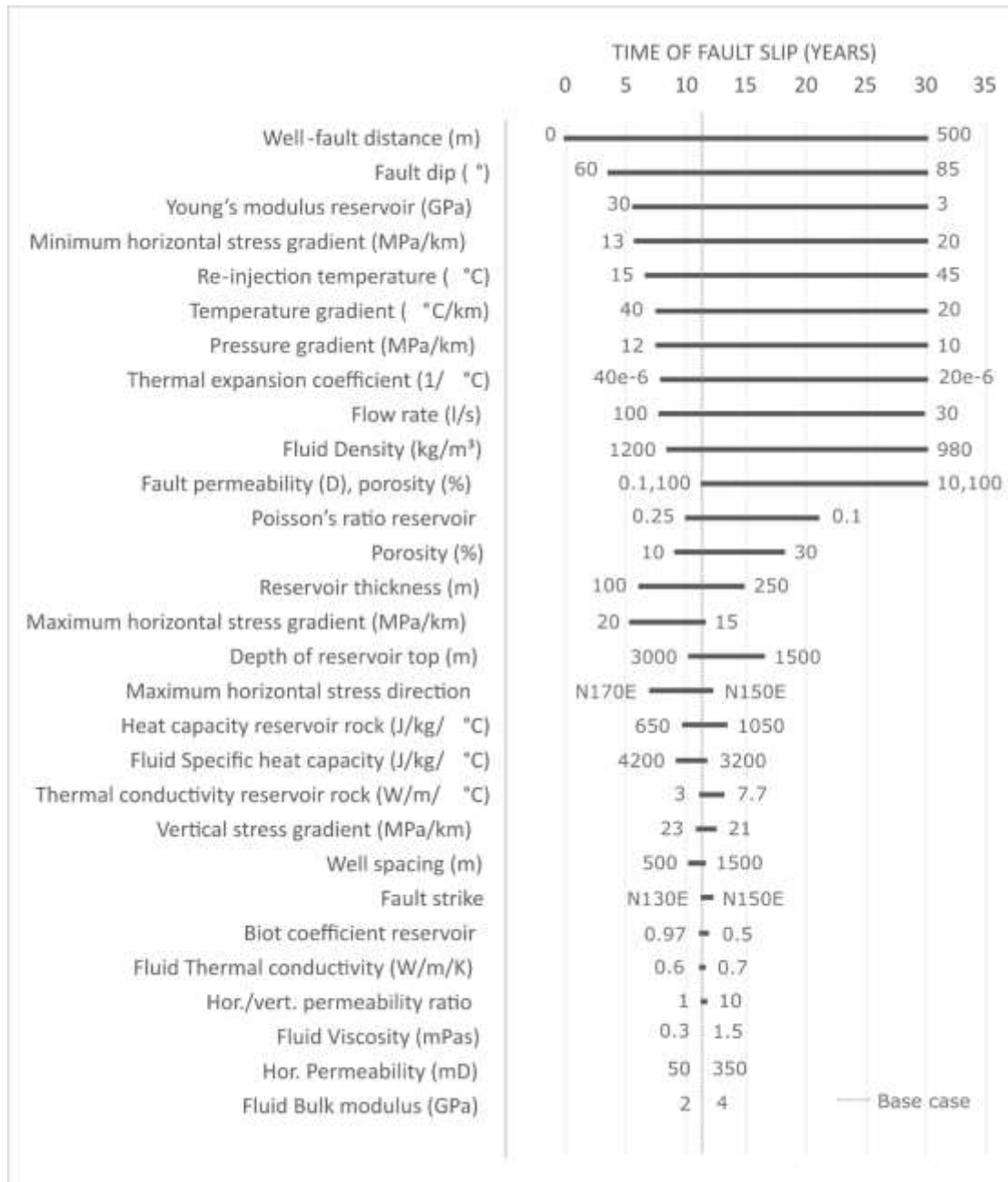
1073



1074

1075 Figure 2: Results of the sensitivity analysis for the fault within the reservoir unit: Fault area with
 1076 slip tendency exceeding the friction coefficient (0.6) of the fault after 30 years of circulation in
 1077 the Slochteren models.

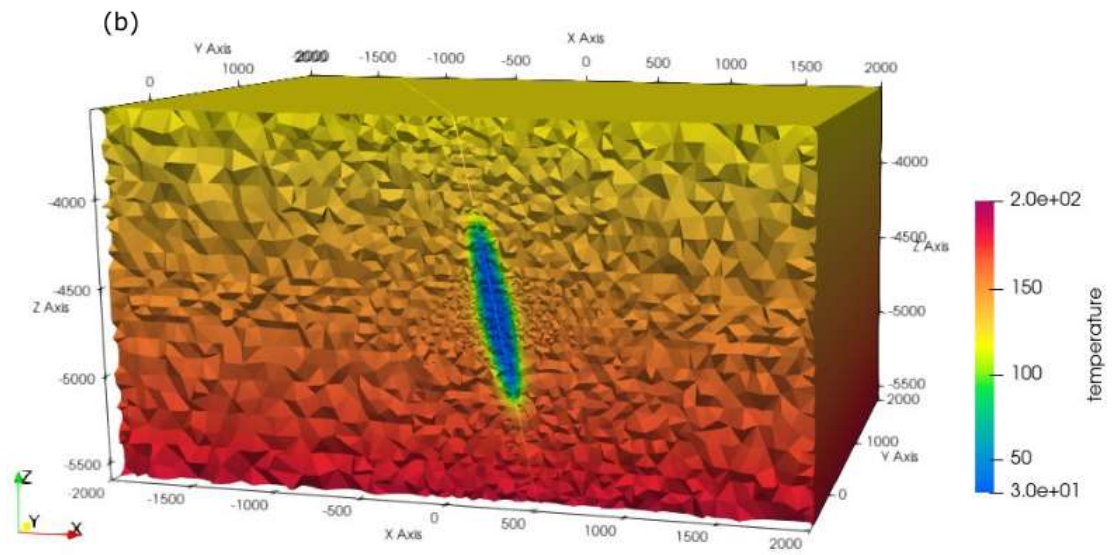
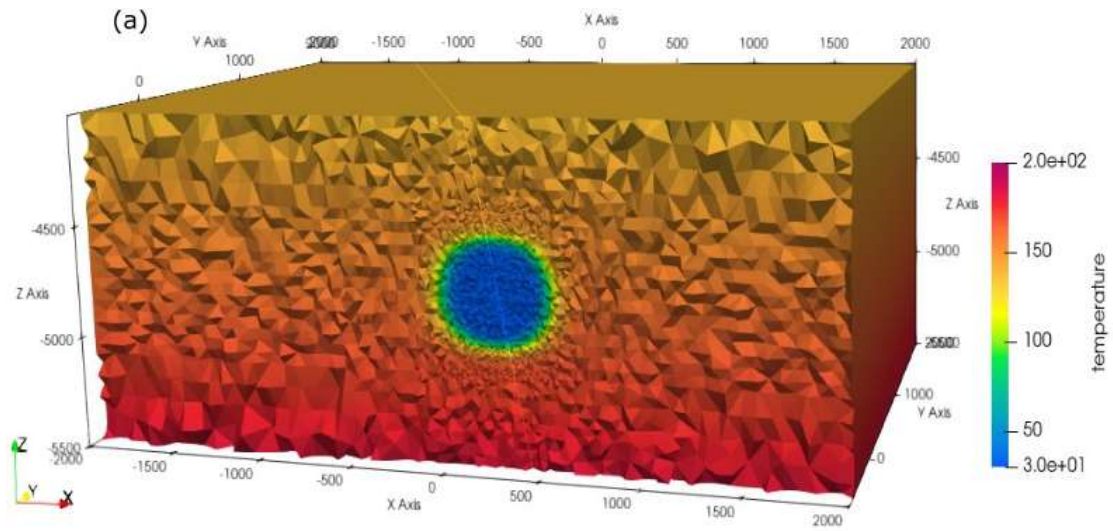
1078



1079

1080 Figure 14: Results of the sensitivity analysis for the fault within the reservoir unit: Time to reach
 1081 the critical slip tendency in the Slochteren models.

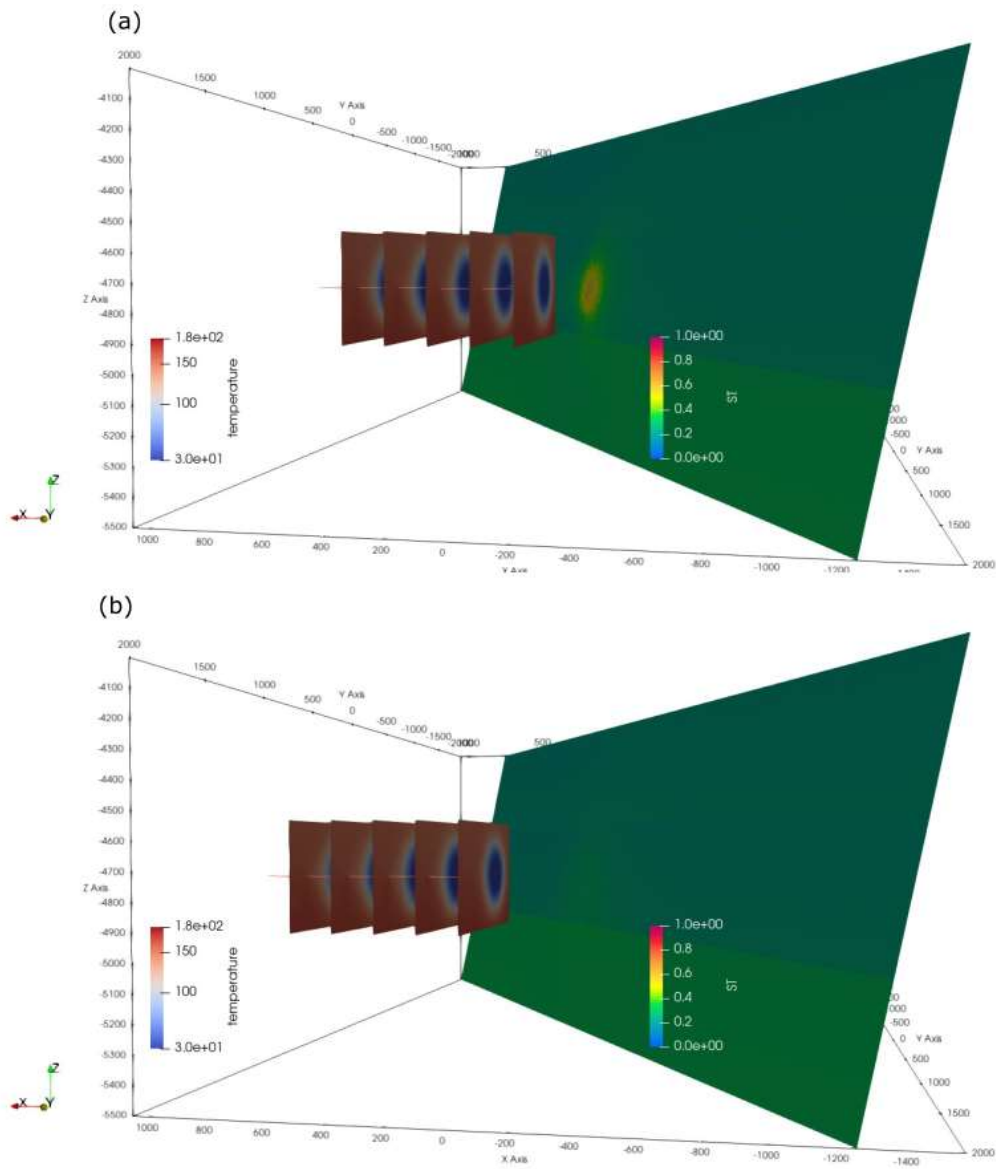
1082



1083

1084 Figure 3: Comparison of temperature distribution after 30 years of circulation in the (a)
 1085 Dinantian fault model and (b) the Dinantian damage zone model.

1086



1087

1088 Figure 4: Comparison of temperature distribution on hydraulic fractures and slip tendency on
 1089 the fault after 30 years of circulation in (a) the Dinantian EGS model with 250 m well-fault
 1090 spacing and (b) 500 m well-fault spacing.

1091

1092 **Supplementary Text S1 – Rate and state friction model of the Slochteren base case scenario**

1093

1094 **S1.1 Rate and state friction model methodology**

1095 To simulate fault reactivation and dynamic slip, we use rate-and-state dependent friction laws in our
1096 models (Dieterich, 1979, 1981; Ruina, 1983). The rate-and-state constitutive equations relate the
1097 evolution of the friction coefficient along the fault to the slip velocity and the change in the state of
1098 the fault surface over time. These principles are based on laboratory tests, in particular velocity-
1099 stepping and slide-hold-slide experiments.

1100 In a general form that quantifies the dependence on slip history with a single state variable, the rate
1101 and state laws can be formulated as follows

$$1102 \quad \mu = f(V, \theta) \quad (S1.1)$$

$$1103 \quad \frac{d\theta}{dt} = g(V, \theta) \quad (S1.2)$$

1104 where μ is the friction coefficient along the fault given as a function of the slip rate, V , and the state
1105 of the fault, θ . The latter parameter is associated with any parameter suitable for the characterization
1106 of the sliding surface, e.g. the average size of the asperity contacts, grain size distribution or porosity
1107 of the fault gouge (Segall, 2010).

1108 An important observation in velocity-stepping experiments is the so called “direct effect”, which is
1109 represented in the rate-and-state laws as the condition

$$1110 \quad \frac{\partial f(V, \theta)}{\partial V} > 0 \quad (S1.3)$$

1111 which means that a sudden increase or decrease of the slip velocity V results in an increasing or
1112 decreasing friction coefficient μ , respectively (Lapusta et al., 2000).

1113 The most commonly used form of equation (S1.1) is

$$1114 \quad \mu(t) = \mu_0 + a \ln\left(\frac{V(t)}{V_0}\right) + b \ln\left(\frac{V_0 \theta(t)}{D_c}\right) \quad (S1.4)$$

1115 where μ_0 is a nominal coefficient of friction (usually $\mu_0 = 0.6$) at the reference slip rate V_0 , a and
1116 b are scaling parameters describing the direct effect and the evolution effect, respectively, and D_c
1117 is the characteristic distance over which the frictional resistance develops after a sudden change in
1118 slip velocity (Segall, 2010).

1119 The state evolution law, eq. (S1.2) has been formulated by several authors in different ways. The
1120 evolution equation we use in this study is the slip law (Ruina, 1983):

$$1121 \quad \frac{d\theta(t)}{dt} = -\frac{V(t)\theta(t)}{D_c} \ln\left(\frac{V(t)\theta(t)}{D_c}\right) \quad (S1.5)$$

1122 Due to the logarithmic form of equation (S1.4), the shear stress is not defined at $V = 0$ along the
 1123 fault, i.e. immediately before reactivation occurs. To solve this problem, regularized rate and state
 1124 equations were suggested by Rice and Ben-Zion (1996), so eq. (S1.4) can be rewritten as:

$$1125 \quad \mu(\theta, V) = a \cdot \operatorname{arcsinh} \left[\frac{V(t)}{2V_0} \exp \left(\frac{\theta(t)}{a} \right) \right] \quad (S1.6)$$

1126 and the slip law (eq. S1.5) takes the form of

$$1127 \quad \frac{\partial \theta(t)}{\partial t} = -\frac{V(t)}{D_c} (\mu(\theta, V) - \mu_{ss}) \quad (S1.7)$$

1128 where $\mu_{ss} = \mu_0 + (a - b) \cdot \ln (V(t)/V_0)$ is the static friction coefficient at $\partial V/\partial t = 0$.

1129

1130 To simulate fault reactivation, stress balance along the fault is described as

$$1131 \quad \tau + \delta\tau_{qs} - \beta_{rad}V = \mu(\theta, V) (\sigma'_N + \delta\sigma_{qs}) \quad (S1.8)$$

1132 where τ and σ'_N are the shear stress and effective normal stress induced on the fault due to
 1133 interaction with the reservoir, $\delta\tau_{qs}$ and $\delta\sigma_{qs}$ are the quasi-static shear stress and normal
 1134 stress components corresponding to the elastic stress transfer due to fault slip. V is slip the
 1135 velocity and β_{rad} is the radiation damping factor. To obtain the shear displacement, u_s , along
 1136 the fault, the system of ordinary differential equations consisting of equations (S1.6), (S1.7)
 1137 and (S1.8) are solved jointly (iteratively) for the slip velocity vector that provides the
 1138 displacement vector along the fault. The system of these equations is implemented in the fully-
 1139 coupled, finite element numerical simulator, GOLEM(Cacace & Jacquey, 2017).

1140

1141 **S1.2 Rate and state friction model setup**

1142 The Rate- and state friction Slochteren _Base Case model is the same as the Slip Tendency
 1143 model except for the additional constitutive fault slip behavior described above. The additional
 1144 model parameters are summarized in Table S9. The dynamic fault slip behavior requires a
 1145 higher time step resolution. Therefore, a different time stepping algorithm was used as
 1146 compared to the ST model.

1147 Most fault gauges tested by Hunfeld et al. (2017) showed velocity-strengthening behavior
 1148 except for some cases of the Basal Zechstein anhydrite-carbonate material at the top of the
 1149 Slochteren reservoir, which thus shows the highest seismogenic potential. However, as
 1150 indicated above, we are using the same Rate-and-state friction (RSF) parameters for the entire
 1151 fault.

1152 Table S9: Rate- and state friction parameters for the Slochteren Base Case model.

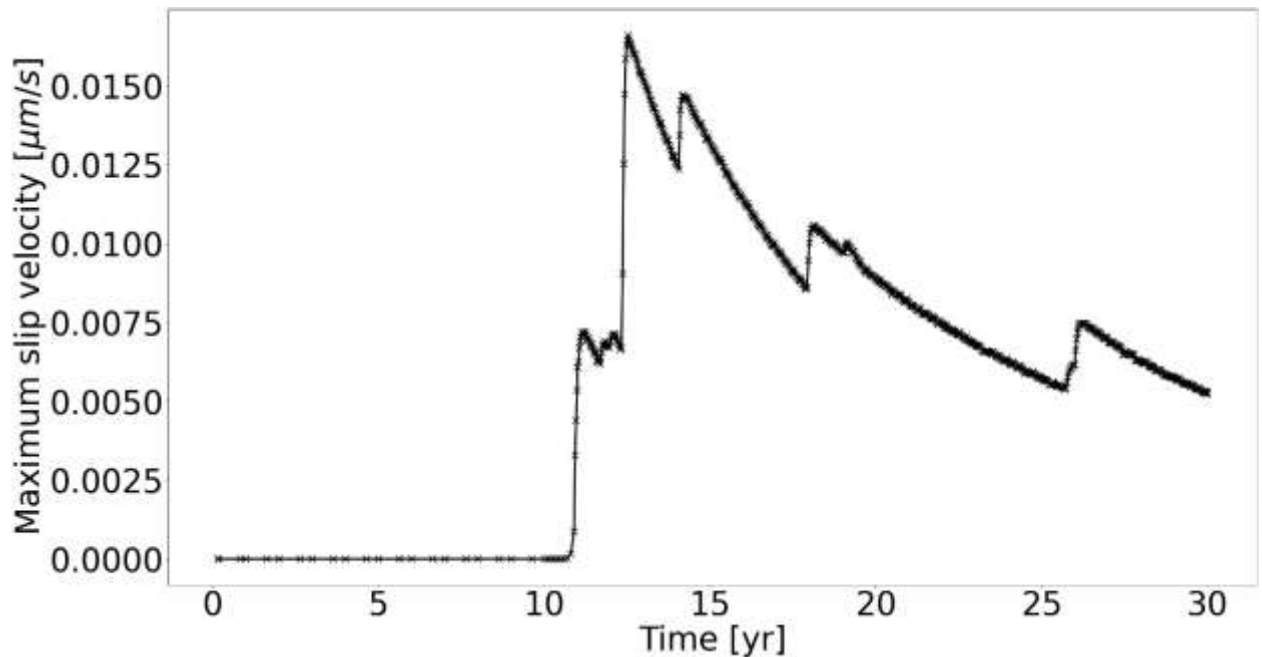
RSF a-value	0.005 (Hunfeld et al., 2017)
-------------	------------------------------

RSF b-value	0.0025 (Hunfeld et al., 2017)
RSF (a-b)-value	0.0025 (Hunfeld et al., 2017)
RSF critical slip distance d_c	1e-5 m (Hunfeld et al., 2017)

1153

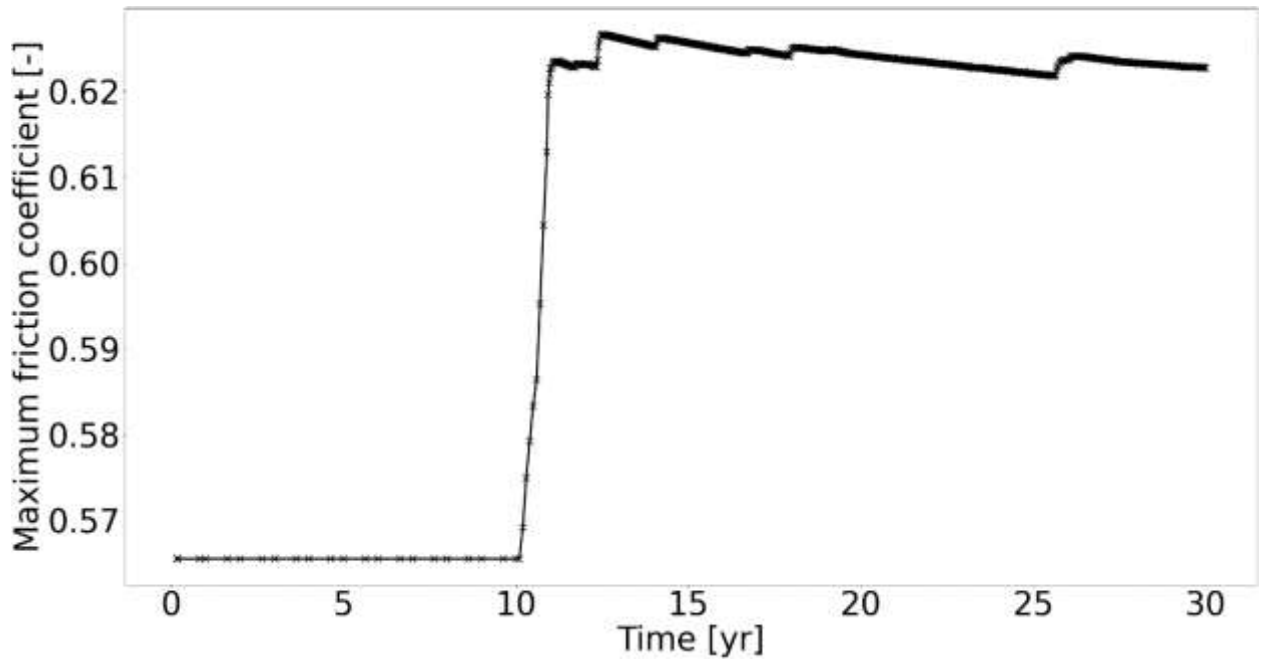
1154 **S1.3 Rate and state friction model results**

1155 In the rate- and state friction model the dynamic fault slip behavior is additionally considered. That
1156 means that the slip velocity (Figure S5), friction coefficient (Figure S2), cumulative seismic moment
1157 (Figure S3) and cumulative slip (Figures S3 and S4) can be evaluated. The RSF parameters
1158 determined by Hunfeld et al. (2017) for Slochteren faults mainly show velocity neutral to velocity
1159 strengthening behavior. The resulting maximum slip velocities are thus extremely low and indicate
1160 aseismic creep-like behavior. That means, while the slip tendency model may indicate that the fault
1161 becomes critically stressed and may slip after ~ 13 years, this slip is likely to be aseismic as a result
1162 of the RSF model. Velocity weakening RSF parameters may show a decisively different behavior.
1163 If the cumulative seismic moment after 30 years shown in Figure S3 would be released in a single
1164 seismic event, this event would have a moment magnitude of 3.6.



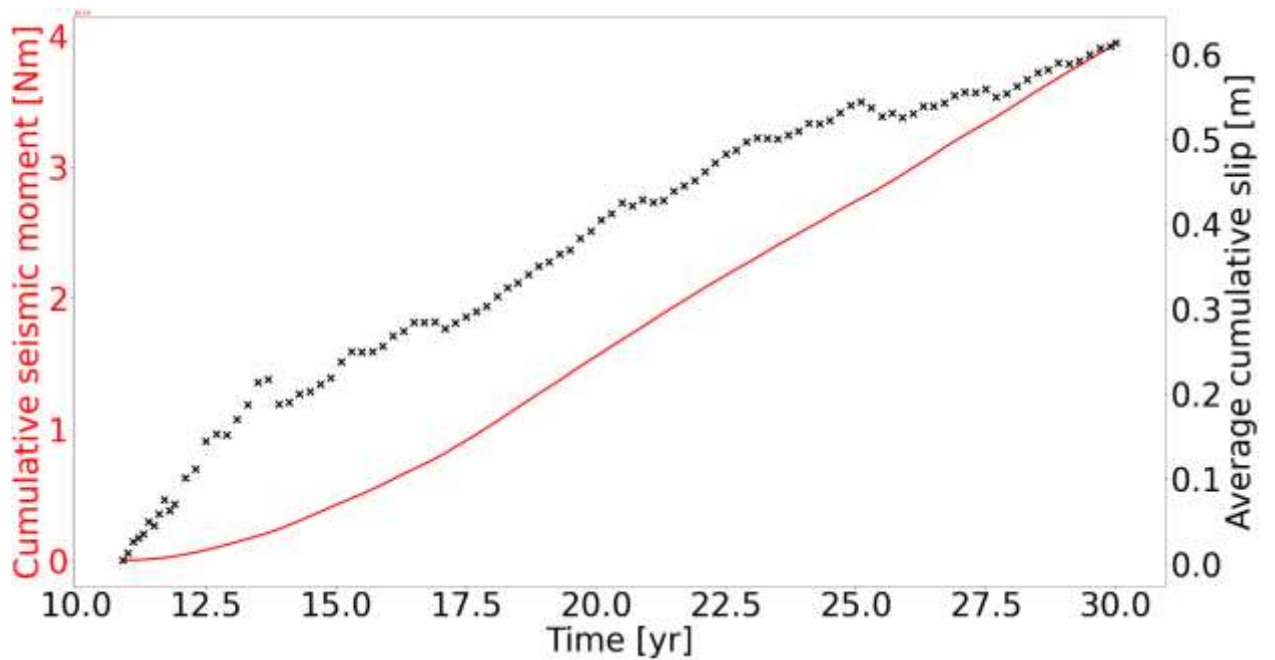
1165

1166 Figure S5: Maximum slip velocity on the fault in the base case Slochteren model during
1167 30 years of fluid circulation.



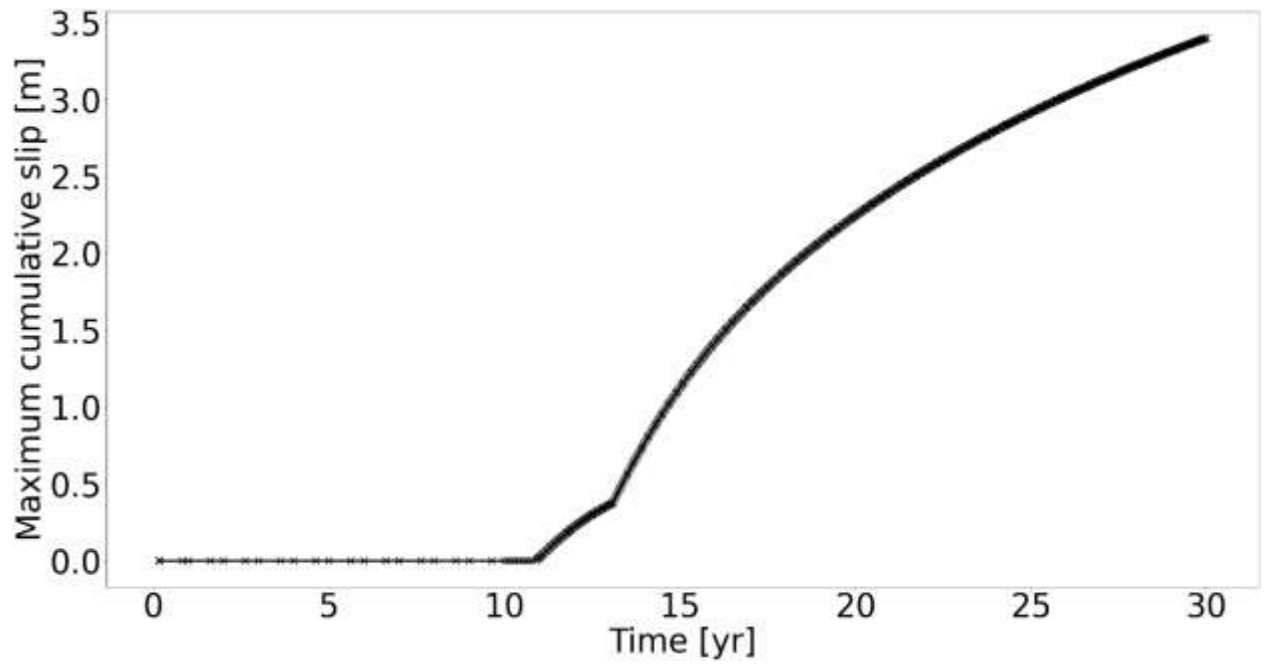
1168

1169 Figure S6: Maximum friction coefficient on the fault in the base case Slochteren model
 1170 during 30 years of fluid circulation.



1171

1172 Figure S7: Cumulative seismic moment and average cumulative slip resulting from the
 1173 RSF base case Slochteren model during 30 years of fluid circulation using the area of
 1174 the fault where the slip tendency is above the friction coefficient of 0.6. Slip starts after
 1175 10 years. If the cumulative seismic moment would be released in a single event, this
 1176 would equal to a Mw 3.6 event.



1177

1178 Figure S8: Maximum cumulative slip resulting from the RSF base case Slochteren
1179 model during 30 years of fluid circulation. Slip starts after 10 years and increases after
1180 ~14 years when the part of the fault intersecting the bottom layer experiences higher
1181 temperature changes and resulting thermal stresses.

1182

1183 **References**

- 1184 *Cacace, M. & Jacquy, A.B.*, 2017. Flexible parallel implicit modelling of coupled thermal–
1185 hydraulic–mechanical processes in fractured rocks. *Solid Earth* **8**: 921–941.
- 1186 *Dieterich, J.H.*, 1979. Modeling of rock friction: 1. Experimental results and constitutive
1187 equations. *Journal of Geophysical Research: Solid Earth* **84**(B5): 2161–2168. doi:
1188 <https://doi.org/10.1029/JB084iB05p02161>
- 1189 *Dieterich, J.H.*, 1981. Constitutive properties of faults with simulated gouge. *Mechanical*
1190 *Behavior of Crustal Rocks* **24**: 103–120.
- 1191 *Hunfeld, L.B., Niemeijer, A.R. & Spiers, C.J.*, 2017. Frictional properties of simulated fault
1192 gouges from the seismogenic groningen gas field under in situ P–T-chemical conditions.
1193 *Journal of Geophysical Research: Solid Earth* **122**(11): 8969–8989.
- 1194 *Lapusta, N., Rice, J.R., Ben-Zion, Y. & Zheng, G.*, 2000. Elastodynamic analysis for slow
1195 tectonic loading with spontaneous rupture episodes on faults with rate- and state-dependent
1196 friction. *Journal of Geophysical Research: Solid Earth* **105**(B10): 23765–23789. doi:
1197 [10.1029/2000JB900250](https://doi.org/10.1029/2000JB900250)
- 1198 *Rice, J.R. & Ben-Zion, Y.*, 1996. Slip complexity in earthquake fault models. *Proceedings of*
1199 *the National Academy of Sciences* **93**(9): 3811–3818. doi: [10.1073/pnas.93.9.3811](https://doi.org/10.1073/pnas.93.9.3811)
- 1200 *Ruina, A.*, 1983. Slip instability and state variable friction laws. *Journal of Geophysical*
1201 *Research: Solid Earth* **88**(B12): 10359–10370. doi: <https://doi.org/10.1029/JB088iB12p10359>
- 1202 *Segall, P.*, 2010. *Earthquake and volcano deformation*. Princeton University Press (Princeton,
1203 N.J): 432 pp.
- 1204
- 1205